HHS Public Access

Author manuscript

Neuron. Author manuscript; available in PMC 2023 March 02.

Published in final edited form as:

Neuron. 2022 March 02; 110(5): 824–840.e10. doi:10.1016/j.neuron.2021.12.031.

Presynaptic autophagy is coupled to the synaptic vesicle cycle via ATG-9

Sisi Yang[1], **Daehun Park**[1,2,6], **Laura Manning**[1], **Sarah E. Hill**[1], **Mian Cao**[1,2,6], **Zhao Xuan**[1], **Ian Gonzalez**[1], **Yongming Dong**[7], **Benjamin Clark**[1], **Lin Shao**[1], **Ifechukwu Okeke**[1], **Agustin Almoril-Porras**[1], **Jihong Bai**[7], **Pietro De Camilli**[1,2,5,6], **Daniel A. Colón-Ramos**[1,3,4,8,9,*]

[1]Program in Cellular Neuroscience, Neurodegeneration and Repair, Departments of Neuroscience and of Cell Biology, Yale University School of Medicine, 260 Whitney Avenue, YSB C167, New Haven, CT 06511, USA

[2]Howard Hughes Medical Institute, Yale University School of Medicine, New Haven, CT 06510, USA

[3]Instituto de Neurobiologìa José del Castillo, Recinto de Ciencias Médicas, Universidad de Puerto Rico, 201 Boulevard del Valle, San Juan, PR 00901, USA

[4]Wu Tsai Institute, Yale University, New Haven, CT 06510, USA

[5]Kavli Institute for Neuroscience, Yale University School of Medicine, New Haven, CT 06510, USA

[6]Aligning Science Across Parkinson's (ASAP) Collaborative Research Network, Chevy Chase, MD 20815, USA

[7]Division of Basic Sciences, Fred Hutchinson Cancer Research Center, Seattle, WA, USA

[8]Twitter: @dacolon

[9]Lead contact

SUMMARY

Autophagy is a cellular degradation pathway essential for neuronal health and function. Autophagosome biogenesis occurs at synapses, is locally regulated, and increases in response

*Correspondence: daniel.colon-ramos@yale.edu.

AUTHOR CONTRIBUTIONS

Conceptualization, S.Y., S.E.H., and D.A.C.-R.; methodology, S.Y., L.M., S.H., M.C., Y.D., J.B., L.S., and D.A.C.-R.; software, L.S.; investigation in *C. elegans*, S.Y., L.M., S.E.H., Z.X., I.G. Y.D., B.C., I.O., and A.A.-P.; investigation in mammalian cells, D.P. and M.C.; formal analysis, S.Y., L.M., D.P., A.A.-P., and Y.D.; writing–original draft, S.Y., L.M., P.D.C., and D.A.C.-R.; writing–review and editing, S.Y., L.M., S.H., Z.X., L.S., D.P., M.C., A.A.-P., J.B., P.D.C., and D.A.C.-R.; visualization, S.Y., L.M., D.P., and D.A.C.-R.; supervision, project administration, and funding acquisition, J.B., P.D.C., and D.A.C.-R.

DECLARATION OF INTERESTS

P.D.C. is a member of the scientific advisory board of Casma Therapeutics.

INCLUSION AND DIVERSITY

One or more of the authors of this paper self-identifies as an underrepresented ethnic minority in science. One or more of the authors of this paper self-identifies as a member of the LGBTQ+ community. One or more of the authors of this paper self-identifies as living with a disability. One or more of the authors of this paper received support from a program designed to increase minority representation in science.

SUPPLEMENTAL INFORMATION

Supplemental information can be found online at https://doi.org/10.1016/j.neuron.2021.12.031.

to neuronal activity. The mechanisms that couple autophagosome biogenesis to synaptic activity remain unknown. In this study, we determine that trafficking of ATG-9, the only transmembrane protein in the core autophagy pathway, links the synaptic vesicle cycle with autophagy. ATG-9-positive vesicles in *C. elegans* are generated from the *trans*-Golgi network via AP-3-dependent budding and delivered to presynaptic sites. At presynaptic sites, ATG-9 undergoes exo-endocytosis in an activity-dependent manner. Mutations that disrupt endocytosis, including a lesion in *synaptojanin 1* associated with Parkinson's disease, result in abnormal ATG-9 accumulation at clathrin-rich synaptic foci and defects in activity-induced presynaptic autophagy. Our findings uncover regulated key steps of ATG-9 trafficking at presynaptic sites and provide evidence that ATG-9 exo-endocytosis couples autophagosome biogenesis at presynaptic sites with the activity-dependent synaptic vesicle cycle.

In brief

Autophagosome biogenesis occurs near synapses and increases with neuronal activity. The mechanisms that couple synaptic autophagy with synaptic activity remain unknown. Yang et al. provide evidence that ATG-9 is on vesicles that undergo activity-dependent exo-endocytosis at synapses, thus coupling autophagosome biogenesis at presynaptic sites with the activity-dependent synaptic vesicle cycle.

Graphical Abstract

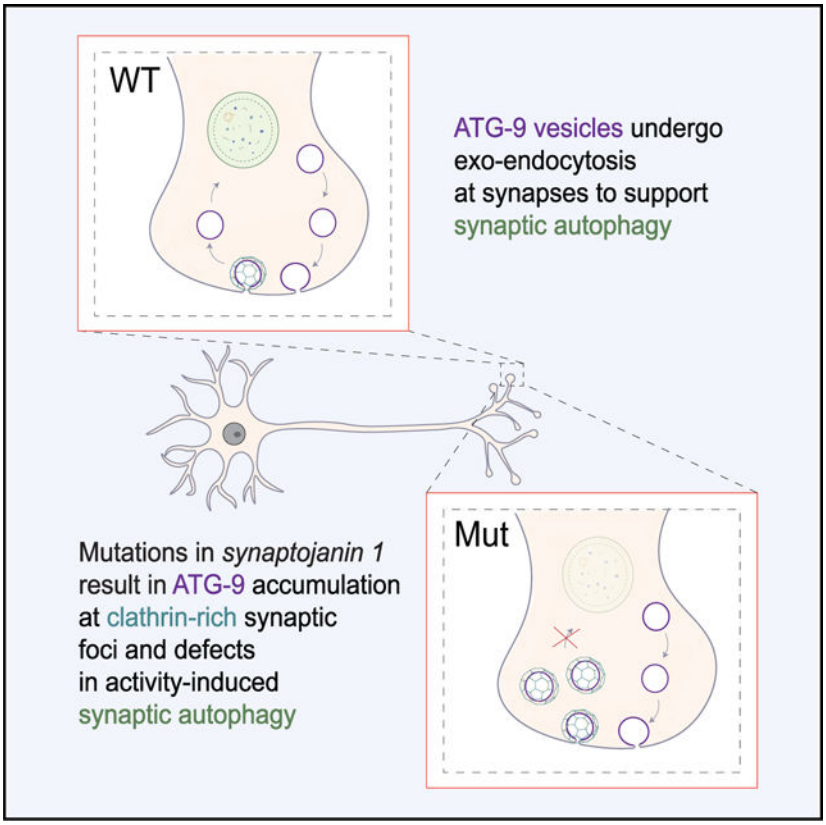

INTRODUCTION

Macroautophagy (herein called autophagy) is an evolutionarily conserved cellular degradative process that is essential for neuronal physiology and survival (Kulkarni et al., 2018; Liang and Sigrist, 2018; Vijayan and Verstreken, 2017; Tsukada and Ohsumi, 1993; Yorimitsu and Klionsky, 2005; Sumitomo and Tomoda, 2021). Neurons are particularly vulnerable to dysfunctional organelles and damaged proteins due to their post-mitotic nature, polarized morphology, and high metabolic activity states during neuronal stimulation (Son et al., 2012; Stavoe and Holzbaur, 2019; Menzies et al., 2017). Autophagy is regulated to cater to these neurophysiological needs. For example, local autophagosome biogenesis occurs near synapses, and autophagosome biogenesis is coupled to the neuronal activity state (Bunge, 1973; Soukup et al., 2016; Maday et al., 2012; Stavoe et al., 2016; Katsumata et al., 2010; Shehata et al., 2012; Hill et al., 2019; Soykan et al., 2021; Wang et al., 2015; Kulkarni et al., 2021; Vijayan and Verstreken, 2017). Disruption of synaptic autophagy has been associated with the accumulation of damaged proteins and organelles, synaptic dysfunction, and neurodegenerative diseases, including Parkinson's disease (Lynch-Day et al., 2012; Zavodszky et al., 2014; Karabiyik et al., 2017; Cheung and Ip, 2009; Hou et al., 2020; Lu et al., 2020).

Molecules that regulate synaptic transmission and function, including proteins involved in synaptic vesicle exo-endocytosis, were reported to regulate autophagy at presynaptic sites (Soukup et al., 2016; George et al., 2016; Vanhauwaert et al., 2017; Murdoch et al., 2016; Kononenko et al., 2017; Binotti et al., 2015; Kuijpers et al., 2021; Andres-Alonso et al., 2021; Hill and Colón-Ramos, 2020; Azarnia Tehran et al., 2018). For example, in *Drosophila*, endophilin A, a protein mainly known for its role in endocytosis, was proposed to directly regulate autophagosome formation by inducing curved membranes that can recruit autophagic machinery (Soukup et al., 2016; Milosevic et al., 2011). Synaptojanin 1, a phosphoinositide phosphatase implicated in the endocytic recycling of synaptic vesicles (SVs) (Cremona et al., 1999; Verstreken et al., 2003; Harris et al., 2000), was also reported to play roles in the control of synaptic autophagy in zebrafish and *Drosophila* (Vanhauwaert et al., 2017; George et al., 2016). Recent studies have revealed links between these canonical endocytic proteins and early-onset Parkinsonism (EOP), suggesting a relationship between the synaptic vesicle cycle (which is tied to synaptic activity), autophagy, and neurodegenerative diseases (Vidyadhara et al., 2019; Trinh and Farrer, 2013; Alegre-Abarrategui and Wade-Martins, 2009; Bandres-Ciga et al., 2019; Schreij et al., 2016; Quadri et al., 2013; Krebs et al., 2013; Zou et al., 2021; Pan et al., 2020). Yet, the mechanistic links underlying the coupling between synaptic activity and autophagosome formation remain unknown.

In this study, we examined the dynamics of ATG-9, the only transmembrane protein of the core autophagy machinery (Noda et al., 2000; Noda, 2017; Webber and Tooze, 2010; Guardia et al., 2020; Lang et al., 2000), at synapses of *C. elegans* and mammalian neurons. ATG-9 cooperates with the lipid transport protein ATG2 in the nucleation of the isolation membrane in nascent autophagosomes (Sawa-Makarska et al., 2020; Gómez-Sánchez et al., 2018) and is thought to promote local autophagosome biogenesis through its role as a lipid scramblase (Guardia et al., 2020; Matoba et al., 2020; Matoba and Noda, 2020; Maeda et

al., 2020; Ghanbarpour et al., 2021). We find that at synapses, ATG-9 links the synaptic vesicle cycle to autophagy. Specifically, we observe that in *C. elegans* neurons, ATG- 9 is delivered to presynaptic sites in vesicles generated by the *trans*-Golgi network (TGN) via AP-3-dependent budding. At presynaptic sites, ATG-9-positive vesicles undergo exo-endocytosis in a synaptic activity-dependent manner. Mutants that disrupt synaptic endocytic traffic, including a *synaptojanin 1/unc-26* allele that mimics a Parkinson's disease mutation, result in abnormal accumulation of ATG-9 in clathrin-rich foci, defects in activity-induced synaptic autophagy, and defects in sustained neurotransmission and locomotory behaviors in aging animals. In mammalian hippocampal neurons, mutations in endocytic proteins similarly result in abnormal ATG-9 accumulation in nerve terminals, indicating conserved mechanisms of ATG-9 trafficking at synapses. Collectively our studies identify regulated dynamics of ATG-9 trafficking at presynaptic sites and provide insights into mechanisms that couple the synaptic vesicle cycle (related to synaptic activity) to presynaptic autophagy.

RESULTS

In *C. elegans*, ATG-9 is transported to synapses in vesicles generated in the *trans*-Golgi network (TGN) via AP-3-dependent budding

Autophagy occurs locally at presynaptic sites in response to synaptic activity, and transmembrane protein ATG-9 plays a critical role in this process (Stavoe et al., 2016; Hill et al., 2019; Soukup et al., 2016; Wang et al., 2015; Shehata et al., 2012). To understand the dynamics of ATG-9 at presynaptic sites, we first examined the *in vivo* localization of ATG-9 in the AIY interneurons of *C. elegans*. AIYs are a pair of bilaterally symmetric cholinergic interneurons, which display a stereotypical distribution of presynaptic specializations along their neurites (White et al., 1986; Colón-Ramos et al., 2007; Altun-Gultekin et al., 2001; Figures 1A, 1B, and 1D). Simultaneous visualization of the presynaptic marker mCherry::RAB-3 and ATG-9::GFP revealed that ATG-9 localization in neurons is compartmentalized and enriched at subcellular structures at the cell body and at presynaptic regions (Stavoe et al., 2016; Figures 1C–1F and 1C′).

To identify the ATG-9-positive structures at synapses, we first developed protocols to locate, image, and reconstruct the ultrastructure of the AIY synaptic Zone 2 region in the context of the nematode brain (see STAR Methods; Figures S1A–S1F; Video S1) and performed post-embedding immunogold electron microscopy on transgenic animals expressing ATG-9::GFP (using anti- bodies directed against GFP). We observed that the majority of the immunogold particles (75%) localized to the presynaptic areas occupied by SVs, with occasional localization of gold particles on the plasma membrane (<10%) (Figures 1G and S1G–S1J). However, the distribution of immunogold particles was generally non-homogeneous in the synaptic vesicle-positive areas. Accordingly, comparison by light microscopy with the localization of mCherry::RAB-3 and of a well-established synaptic vesicle integral membrane protein, SNG-1/synaptogyrin::BFP, revealed strong colocalization between mCherry::RAB-3 and SNG-1::BFP but subtle differences between the colocalization of these two synaptic vesicle proteins and ATG-9::GFP (Figures 1H–1K and S1K–S1M), consistent with the immuno-EM observations and suggestive that ATG-9 is enriched on a subpopulation of vesicles.

To determine the site of ATG-9 localization within the cell soma, we co-expressed either ATG-9::mCherry or ATG-9::GFP with other organelle markers. We observed that ATG-9::GFP was concentrated at sites that overlapped with *trans*-Golgi marker TGN-38::mCherry and that ATG-9::mCherry was directly adjacent to the medial/*cis*-Golgi marker AMAN-2::GFP but did not overlap with other organelles markers (Figures 1L–1R, 1L′, and S2A–S2H). These findings, which are consistent with observations from yeast and mammalian culture cells (Noda, 2017; Webber et al., 2007; Ohashi and Munro, 2010; Yamamoto et al., 2012; Young et al., 2006), indicate a *trans*-Golgi-specific enrichment of ATG-9 at the neuronal cell body *in vivo*.

The TGN is the compartment where vesicles destined for transport to distinct subcellular locations are packaged. In vertebrates, adaptor protein complex 4 (AP-4) is particularly important in exporting transmembrane protein ATG9A from the Golgi apparatus, and mutations in AP-4 have been associated with neurological disorders (De Pace et al., 2018; Mattera et al., 2017; Ivankovic et al., 2020; Ebrahimi-Fakhari et al., 1993; Behne et al., 2020). However, in *C. elegans* and other invertebrates, no orthologues of AP-4 have been characterized. Which proteins are then required for the biogenesis of ATG-9-positive vesicles?

We tested mutants for AP complexes UNC-101/AP-1, DPY-23/AP-2, and AP-3 (Park and Guo, 2014; Nakatsu and Ohno, 2003; Margeta et al., 2009; Xuan et al., 2021; Figures S2N–S2Q) and determined that putative null alleles for the three AP-3 complex subunits (apb-3/β3-adaptin, apm-3/μ3, apd-3/δ-adaptin) abnormally resulted in higher ratio between ATG-9 at the cell body and synapses (Figures 1S–1U, 1X, and 1Y). Interestingly, the *apb-3* allele did not affect the localization of the synaptic vesicle proteins SNG-1 or RAB-3 to presynaptic sites, suggesting that the observed decrease of ATG-9 at synapses is not due to a general problem in synaptic vesicle biogenesis (Figures 1V, 1W, 1Z, and S2I–S2M). Together, our findings reveal that *in vivo* in *C. elegans* neurons, enrichment of ATG-9 at presynaptic sites results from AP-3-mediated export of ATG-9-positive vesicles at the TGN.

ATG-9 undergoes exo-endocytosis at presynaptic sites

The observed localization of ATG-9 to vesicles at presynaptic sites, and its occasional localization in the axonal plasma membrane, raised the possibility that this protein may be a component of vesicles that undergo exo-endocytosis. To address this possibility, we imaged ATG-9 synaptic localization in *C. elegans* neurons in mutants with disrupted exo-endocytic trafficking at presynaptic sites (Harris et al., 2000; Watanabe et al., 2014; Südhof, 1995; Saheki and De Camilli, 2012; Schuske et al., 2003; Li et al., 2016; Figure 2A). We observed that endocytic mutants *unc-26(s1710)/ unc-26(e205)/synaptojanin 1, unc-57(ok310)/endophilin A*, and temperature-sensitive *dyn-1(ky51)/dynamin 1* displayed defects in ATG-9 localization at synapses (Figures 2C–2H). For example, in the AIY interneurons presynaptic-rich region (termed Zone 2 [Colón-Ramos et al., 2007]), the ATG-9::GFP signal is distributed across this presynaptic area (Figure 2C). However, in all the endocytic mutants examined, more than 65% of animals displayed abnormal accumulation of ATG-9::GFP into multiple subsynaptic foci (Figures 2D–2H and S3A). To quantify the genetic expressivity of the phenotype, we defined an index for ATG-9

mislocalization (STAR Methods). We found that in the endocytic mutants there was a significant difference in the subsynaptic localization of ATG-9, with more than 1.7-fold increase in the index of ATG-9 mislocalization, reflecting abnormal enrichment at discrete foci within the presynaptic regions for loss-of-function alleles of *unc-26(s1710)*, *unc-57(ok310)*, and temperature-sensitive allele *dyn- 1(ky51)* (Figure 2K). Expressing *unc-26* cDNA cell specifically in the AIY interneurons of *unc-26(e205)* mutants rescued ATG-9 defects at the synapse, indicating that UNC-26 acts cell autonomously in neurons to prevent abnormal ATG-9 accumulation at subsynaptic foci (Figures S3E–S3G).

If the accumulation of ATG-9 at abnormal foci in endocytic mutants is due to abnormal endocytic traffic, then mutants in exocytosis should suppress this phenotype. To test this hypothesis, we examined putative null alleles *unc-13(s69)/Munc1*3 and *unc-18(e81)/Munc18*, which encode essential components of synaptic vesicle exocytosis (Hata et al., 1993; Richmond et al., 1999). Single mutants of *unc-13(s69)* and *unc-18(e81)* did not disrupt ATG-9 localization (Figures S3A, S3H, and S3I). Importantly, double mutants of *unc-13(s69);unc-26(e205)* and *unc-18(e81);unc-26(s1710)* suppressed the *unc-26/synaptojanin 1* mutant phenotype, indicating that the accumulation of ATG-9 at abnormal foci depends on synaptic vesicle exocytosis (Figures 2I–2K and S3A).

Our genetic perturbations in *C. elegans* are consistent with ATG-9-positive vesicles undergoing exo-endocytosis at presynaptic sites. To better examine this, we imaged ATG-9 dynamics in a loss-of-function allele of *phosphofructokinase 1/pfk-1.1(gk922689)*. The absence of phosphofructokinase, like the absence of other glycolytic proteins, results in impaired synaptic vesicle endocytosis during transient hypoxia (Jang et al., 2016). Through the use of a microfluidic device that allows precise control of transient cycles of normoxia and hypoxia, we can temporally control the endocytic reaction (Jang et al., 2021). We examined ATG-9 localization in the synaptic Zone 3 region (Figures 2B and 2B″). We observed that in *pfk-1.1(gk922689)* mutants, transient inhibition of endocytosis during transient hypoxia correlated with ATG-9 re-localization from discrete presynaptic clusters in the synaptic Zone 3 region, to a more diffuse distribution, consistent with what would be expected if ATG-9 were trapped at the plasma membrane due to short-term defects in endocytosis (Figures 2L and S3J). Conversely, removing the endocytic block by shifting to normoxia rescued the localization of ATG-9 to the presynaptic clusters (Figure 2L). Moreover, inhibition of exocytosis in *unc-13(s69)* mutants suppressed the transient hypoxia-induced ATG-9 re-localization in *pfk-1.1(gk922689)* mutants (Figures S3K–S3L). Our data indicate that ATG-9-positive vesicles undergo exo-endocytosis at presynaptic sites by using the synaptic vesicle cycling machinery.

Biochemical evidence that ATG-9 travels to and from the plasma membrane

Our results are consistent with published evidence that ATG-9 can be exposed at the cell surface and then re-internalized by endocytosis in mammalian fibroblastic cells, as revealed by immunocytochemistry following perturbation of a critical endocytic factor, dynamin, either pharmacologically or by dominant interference (Puri et al., 2013; Feng and Klionsky, 2017; Zhou et al., 2017). To obtain direct biochemical evidence for ATG-9 exo-endocytosis, we performed cell surface biotinylation experiments (with Sulfo-NHS-LC-

Biotin) in tamoxifen-inducible dynamin 1 and 2 double-knockout (DKO) mouse fibroblasts (Ferguson et al., 2009). A pool of ATG9A, and of transferrin receptor (TfR) as a control, was detected at the plasma membrane in control fibro-blasts, and these pools were enhanced in fibroblasts where the expression of dynamin 1 and 2 had been suppressed by tamoxifen (Figures 2M, 2N, and S5A–S5C), providing biochemical evidence that ATG-9 travels to and from the plasma membrane and that its internalization depends on endocytic proteins. These results, together with our light microscopy findings, support a model that ATG-9 cycles, by exo-endocytosis, between intracellular vesicular compartments and the plasma membrane.

ATG-9 mislocalization phenotypes can be predictably altered by manipulating the AIY activity state

Local synaptic autophagy increases with increased neuronal activity states (Hill et al., 2019; Soukup et al., 2016; Katsumata et al., 2010; Shehata et al., 2012; Soykan et al., 2021; Kulkarni et al., 2021). To determine if ATG-9 exo-endocytosis links the activity state of neurons with autophagy, we examined if the mislocalization phenotype of ATG-9 could be modified based on the neuronal activity state.

AIY neurons in *C. elegans* are part of the thermotaxis circuit, which allows animals to navigate toward their cultivation temperature, and the activity state of AIY increases based on the cultivation temperature at which the organism is reared (Hawk et al., 2018; Figures S4A–S4C). When we examined the ATG-9 phenotype in *unc-26(s1710)/synaptojanin 1* mutants under these conditions, we observed that the penetrance of the ATG-9 phenotype similarly varied depending on the cultivation temperature of the animals, and that the temperature-dependent increases of abnormal ATG-9 foci in *unc-26(s1710)/synaptojanin 1* mutant animals were suppressed by the exocytosis mutant *unc-13(s69)* (Figure 3A). Moreover, chemo-genetic silencing of AIY through cell-specific expression of the heterologous histamine-gated chloride channel (HisCl) in AIY (Pokala et al., 2014; Hill et al., 2019) partially suppressed temperature-related abnormal increases in ATG-9 foci observed for *unc-26(s1710)/synaptojanin 1* mutants (Figures 3B, 3C, and 3F). Similar results were observed when we expressed the inhibitory light-driven chloride pump (NpHR) (Li et al., 2014; Zhang et al., 2007) in the AIYs of *unc-26(s1710)/synaptojanin 1* mutants and activated them with light (Figures 3D–3F).

These chemo-genetic, optogenetic, and physiological approaches to manipulate AIY activity state support the hypothesis that the ATG-9 mislocalization phenotype can be manipulated by increasing or decreasing neuronal activity and that ATG-9 exo-endocytosis responds to the synaptic activity state.

In *unc-26/synaptojanin 1* mutants, ATG-9 accumulates at presynaptic, clathrin-rich sites

To identify ATG-9-positive structures in *unc-26/synaptojanin 1* mutants, we performed electron microscopy studies of transgenic animals expressing ATG-9::GFP in *unc-26/synaptojanin 1* mutants (Figures 4A, 4B, and S6). Staining against ATG-9::GFP, we observed fewer gold particles in *unc-26(e205)* mutants than in wild-type (WT) synapses, consistent with confocal imaging data that showed reduced intensity of ATG-9::GFP at *unc-26* mutant synapses (Figures S3B–S3D). ATG-9 labeling, although reduced,

concentrated near vesicular structures within the cross-sectional areas of Zone 2 (Figures 4A, 4B, and S5D).

Synaptojanin 1 plays conserved roles in clathrin-mediated endocytosis, and in *C. elegans*, *Drosophila*, and vertebrates, mutations in synaptojanin 1 result in the accumulation of clathrin-coated, abnormal endocytic intermediates (Harris et al., 2000; Verstreken et al., 2003; Cremona et al., 1999; Kim et al., 2002; Milosevic et al., 2011; Saheki and De Camilli, 2012; Figure S6). To determine whether ATG-9 colocalized with these intermediates, we simultaneously imaged ATG-9::GFP and BFP::CHC-1/Clathrin Heavy Chain in the AIY interneurons of WT animals and *unc-26(s1710)/synaptojanin 1* mutant animals (Figures 4C–4E, 4L, and S5M–S5O). We found that in the *unc-26(s1710)* mutants, CHC-1 synaptic signal increased, localized to abnormal foci at synapses (Figures 4D and S5E–S5H), and colocalized with abnormal ATG-9 foci (Figures 4C–4E and 4L). We note that, although synaptojanin 1 is also required for the endocytic traffic of synaptic vesicle proteins, we did not observe synaptic vesicle proteins in a pattern similar to the clathrin-rich structures, indicating that mutations in endocytic proteins affect ATG-9 and a *bona fide* synaptic vesicle protein differently (Figures 4F–4H, 4L, and S5I–S5L). Moreover, simultaneous imaging of ATG-9::mCherry and of the autophagosome marker, GFP::LGG-1/Atg8/GABARAP (Alberti et al., 2010; Manil-Ségalen et al., 2014; Wu et al., 2015; Stavoe et al., 2016; Hill et al., 2019) in the *unc-26(s1710)/synaptojanin 1* mutants did not reveal ATG-9 enrichment on the LGG-1-containing compartments, which usually corresponds to nascent autophagosomes (Alberti et al., 2010; Manil-Ségalen et al., 2014; Wu et al., 2015; Stavoe et al., 2016; Hill et al., 2019) (however, they sometimes appeared adjacent to each other [Figures 4I–4L and S5P–S5R]).

In autophagy mutants, ATG-9 accumulates into endocytic intermediates at presynaptic sites

The critical role of ATG-9 in autophagy predicts that disruption of autophagy should impact ATG-9 localization (Reggiori et al., 2004; Sekito et al., 2009; Lu et al., 2011). Thus, we also examined ATG-9 localization in mutants with disrupted autophagy (Figure 5A). In loss-of-function alleles *unc-51(e369)/ATG1*, *epg-9(bp320)/Atg101*, *atg-13(bp414)/epg-1*, and *epg-8(bp251)/Atg14* (Crawley et al., 2019; Liang et al., 2012; Huang et al., 2013) that affect early steps of autophagosome initiation, we observed abnormal focal accumulation of ATG-9 at presynaptic sites (Figures 5B–5G). Similar to *unc-26* mutants, the abnormal focal accumulation of ATG-9::GFP in *epg-9(bp320)* autophagy mutants colocalized with clathrin heavy chain BFP::CHC-1 (Figures S7A–S7C). We also observed that the penetrance of the ATG-9 phenotype in *epg-9(bp320)* mutants varied according to the cultivation temperature of the animals (which relates to the activity state of the AIY interneurons (Hawk et al., 2018; Figures 5H and S4A–S4C). Our findings indicate that disruption of either the endocytic or autophagy machinery shares a phenotype in the abnormal accumulation of ATG-9 at synapses and supports our model that ATG-9 trafficking links the synaptic vesicle cycle and the autophagy pathway.

Disrupted ATG-9 exo-endocytosis in *unc-26/ synaptojanin 1* mutants is associated with defects in activity-induced synaptic autophagy

To relate changes in ATG-9 localization at the synapse with activity-induced increases in synaptic autophagy, we examined LGG-1/Atg8/GABARAP puncta in mutant backgrounds that affect exo-endocytosis at the synapse. Consistent with the previous findings, we observed that the average number of LGG-1 puncta increased when the WT animals were cultivated at 25°C, a condition known to increase the activity state of the AIY neurons (Hawk et al., 2018) (Figures S4A–S4C) and synaptic autophagy (Hill et al., 2019) (Figures 5M, S7D, and S7F). Inhibiting exocytosis (in *unc-13(s69)* mutants) or disrupting the autophagy pathway (in *atg-9(wy56)* mutants) eliminated the capacity of the neurons to increase synaptic autophagy in response to increases in the cultivation temperature (Figure 5M). The LGG-1 puncta in *unc-26(s1710)* mutants could not be suppressed by autophagy mutants nor did it increase in response to cultivation temperatures, suggesting that the observed LGG-1 puncta in the *unc-26(s1710)* mutants are not *bona fide* functional autophagosomes (Figures 5M, S7E, and S7G).

To better examine the specific role of ATG-9 trafficking in synaptic autophagy, we disrupted ATG-9's capacity to undergo exo-endocytosis by deleting a conserved YXXØ (Ø is a hydrophobic amino acid) sorting motif in ATG-9 (YQQID sequence in *C. elegans*, hereinafter referred to as ΔAP). The YXXØ sorting motif mediates ATG-9 interactions with endocytosis adaptor proteins AP-2 (Imai et al., 2016; Figure 5I). In mouse cultured cells, disruption of this sorting motif in ATG-9 results in abnormal ATG-9 trafficking, in its abnormal accumulation in endosomes, and in autophagy defects (Imai et al., 2016; Popovic and Dikic, 2014). Examination of animals expressing ATG-9(ΔAP)::GFP cell specifically in AIY revealed that ATG-9(ΔAP) was still transported to synapses, where it abnormally localized to presynaptic foci (Figures 5J–5L; we also observed accumulation of ATG-9 foci, likely corresponding to Golgi apparatus, at the cell body). This is consistent with our observations on the requirement of endocytic proteins for ATG-9 sorting at synapses and with previous findings that demonstrated the requirement of adaptor proteins (APs) for ATG-9 sorting at the Golgi (via AP-4) (Mattera et al., 2017), the plasma membrane, and endosomes (via AP-2) (Popovic and Dikic, 2014; Imai et al., 2016). In a CRISPR-engineered allele harboring this mutation *atg-9(ΔAP)*, we observed a ~2- to 3-fold decrease in LGG-1-containing puncta (and therefore autophagosomes) in the AIY neurites, revealing defects in synaptic autophagosome formation in *atg-9(ΔAP)* mutants defective in sorting (Figure 5M).

Abnormal accumulation of ATG9A in nerve terminals of mammalian neurons with mutations in endocytic proteins

Next, we investigated the localization of ATG9A in nerve terminals of hippocampal neuronal cultures of mice double KO for dynamin 1 and 3 (the two neuronally enriched dynamin isoforms) and KO for synaptojanin 1 (SJ1) (the neuronally enriched synaptojanin isoform) (Raimondi et al., 2011; Cremona et al., 1999; Ferguson and De Camilli, 2012). Synapses of both genotypes are characterized by a massive accumulation of synaptic vesicle endocytic intermediates, endocytic pits (in the case of *dynamin* mutants), and clathrin-coated vesicles (in the case of *synaptojanin 1* mutants) (Raimondi et al., 2011; Hayashi et al.,

2008; Ferguson et al., 2007; Milosevic et al., 2011). Accordingly, we observed stronger synaptic staining, visualized with anti-amphiphysin 2, in dynamin 1 and 3 DKO neurons (Dyn1/3 KO) and SJ1 KO neurons than in WT controls (Figures 6C, 6F, 6I, 6L, and S8A). Importantly, anti-ATG9A immunofluorescence also revealed a striking accumulation at a subset of mutant synapses relative to WT synapses (Figures 6B, 6E, 6H, and 6K). Such 'hot spots' of ATG9A colocalized with amphiphysin 2 immunoreactivity, confirming the synaptic localization of anti-ATG9A (Figures 6A–6L). However, the number of synaptic puncta were more numerous for amphiphysin 2 than for ATG9A, suggesting a heterogeneous localization of ATG9A at synapses, or a different impact of the perturbation of dynamin and SJ1 on ATG9A in different neurons.

A mutation in *unc-26/synaptojanin 1* associated with early-onset Parkinsonism (EOP) leads to abnormal focal accumulation of ATG-9 in presynaptic nerve terminals

A missense mutation in *synaptojanin 1(R258Q)* is associated with EOP (Quadri et al., 2013; Krebs et al., 2013). Introduction of the same mutation in mouse and *Drosophila* was reported to affect endocytic trafficking and autophagosome maturation at synapses (Cao et al., 2017; Vanhauwaert et al., 2017). The mutant position, which impairs the PI4P phosphatase catalytic activity of the Sac1 domain, is conserved in *C. elegans unc-26(R216Q)* (Figure 7A). We asked if this mutation also affects ATG9A localization at synapses.

Immunofluorescence staining of endogenous ATG9A in hippocampal cultures generated from SJ1RQKI mice revealed abnormal ATG9A accumulations that colocalized with focal enrichment of amphiphysin 2 foci at a subset of synapses (Figures 7B–7E and S8A) and were similar to those observed in SJ1 KO neurons (Figures 6J–6L and S8A). We had previously shown that both in $SJ1^{RQ}$KI and in SJ1 KO neurons such presynaptic accumulation of endocytic factors is more prominent at inhibitory than at excitatory presynaptic terminals, as revealed by a greater colocalization with vesicular GABA transporter (vGAT) (a marker of inhibitory presynaptic terminals) than with vGlut1 (a marker of excitatory presynaptic terminals) (Hayashi et al., 2008; Cao et al., 2017). Most likely this difference is due to the higher level of tonic activity of inhibitory synapses (Luthi et al., 2001). Accordingly, hotspots of ATG9A and amphiphysin 2 occurred selectively at vGAT-positive synapses (Figures 7F–7I and 7F′–7I′).

Likewise, in *unc-26(R216Q)* mutant *C. elegans*, ATG-9::GFP was abnormally localized to subsynaptic foci enriched with clathrin and which resembled those observed in *unc-26(e205)/unc-26(s1710)/SJ1* null alleles, albeit at a lower penetrance, consistent with partial loss of function (Figures 7J, 7K, S8B, and S8O–S8Q). We also observed that the *unc-26(R216Q)* allele, contrary to the loss-of-function allele, did not produce obvious changes in the localization of the synaptic vesicle proteins SNG-1 or RAB-3 at presynaptic Zone 3 regions (Figures S8D–S8I), suggesting that the *unc-26(R216Q)* allele differentially affects ATG-9 localization and synaptic vesicle protein localization. Similar with the *unc-26(s1710)* null mutants, the penetrance of *unc-26(R216Q)* mutants increased with the cultivation temperatures that are associated with higher synaptic activity states (Figure S8J). These findings are consistent with *Drosophila* studies indicating that the *unc-26(R216Q)* Parkinson's disease mutation impairs autophagy at the synapse (Vanhauwaert et al., 2017)

and in this study are extended to show an impact of this lesion on ATG-9 trafficking at presynaptic sites.

Another Sac domain-containing protein, Sac2/INPP5F (Figure 7A), is located within a Parkinson's disease risk locus identified by genome-wide association studies (Blauwendraat et al., 2019; Nalls et al., 2014). We examined two putative null alleles of *sac-2* in *C. elegans*, *sac-2(gk927434)* and *sac-2(gk346019)*, for phenotypes in ATG-9 localization. Although single mutants of *sac-2* do not affect ATG-9 localization (data not shown), *sac-2(gk927434);unc-26(s1710)* and *sac-2(gk346019);unc-26(s1710)* double mutants enhance the abnormal localization of ATG-9 in *unc-26(s1710)* single null allele, suggesting that *sac-2* and *unc-26/synaptojanin 1* function synergistically in mediating ATG-9 trafficking at synapses (Figures 7L, 7M, and S8C), consistent with previous findings showing that Sac2 and synaptojanin 1 have overlapping roles in the endocytic pathway at synapses (Cao et al., 2020), and indicating that lesions associated with EOP in endocytic mutants result in abnormal ATG-9 accumulation.

To understand the impact of the *unc-26(R216Q)* lesion on aging of the synapses, we recorded excitatory postsynaptic currents (EPSCs) at neuromuscular junctions in early-life (day 1) and mid-life (day 7) adult worms. We found that the amplitude of evoked EPSCs (Figure 7N) and the frequency of endogenous EPSCs (Figures 7O, S8M, and S8N) were significantly decreased in day 7 *unc-26(R216Q)* mutants, when compared with those in day 7 WT worms. By contrast, levels of synaptic currents were identical in day 1 WT and *unc-26(R216Q)* animals (Figures S8K–S8N). These findings indicate that the *unc-26(R216Q)* lesion disrupts synaptic activity in an age-dependent manner. Consistent with an accelerated decay of synaptic physiology, *unc-26(R216Q)* mutants displayed decreased locomotion rates in day 7 adult worms but not in day 1 mutant animals (Figure 7P). Our findings are consistent with a prior report demonstrating neurological manifestations of the $SJ1^{RQ}KI$ lesion in mice (Cao et al., 2017). They now demonstrate that the *unc-26(R216Q)* lesion in *C. elegans* promotes abnormal accumulation of ATG- 9 and accelerates age-dependent decay of synaptic physiology and behavior.

DISCUSSION

In *C. elegans*, ATG-9 exits the Golgi complex in an AP-3 dependent manner. The *C. elegans* AP-3 protein complex is structurally and mechanistically related to the mammalian AP-4 complex, which in vertebrates is required for transport of ATG-9 from the TGN to the peripheral cytoplasm (Rout and Field, 2017; Dell'Angelica, 2009; Ivankovic et al., 2020; Mattera et al., 2017). Invertebrates, including *C. elegans*, do not have AP-4 complexes. AP-3 is a sorting complex best known for its role in regulating trafficking to lysosome-related organelles (Odorizzi et al., 1998; Cowles et al., 1997; Stepp et al., 1997), and our findings extend our understanding of AP-3 roles in regulating lysosome-mediated cellular processes, including autophagy via the sorting ATG-9. It remains to be determined if AP-3 plays conserved roles with AP-4 in ATG-9 trafficking in mammalian neurons.

ATG-9-enriched vesicles at the synapse might represent a partially distinct subpopulation of vesicles. In nerve terminals, as shown by our EM analyzes, the bulk of ATG-9 is localized

in small vesicles. Although one cannot identify molecularly distinct vesicle populations based on size and morphological appearance in EM, interestingly the immunogold staining suggests a predominant concentration of ATG-9 on a subpopulation of vesicles. Likewise, fluorescent microscopy revealed only partial overlap in nerve terminals between the distribution of ATG-9 and of the intrinsic membrane protein of SVs, SNG-1/synaptogyrin. Consistent with these findings, ATG-9 was identified by mass spectrometry in a synaptic vesicle fraction (Boyken et al., 2013; Chantranupong et al., 2020; Taoufiq et al., 2020), suggesting compositional overlap between ATG-9 vesicles and *bona fide* SVs. We speculate that ATG-9-containing vesicles constitute a distinct class of synaptically localized vesicles, which might partially overlap in protein composition with canonical, neurotransmitter releasing vesicles.

Synaptically localized ATG-9-containing vesicles undergo exo-endocytosis. We demonstrate that their exocytosis is *unc-13/unc-18*-dependent and that their endocytic trafficking is affected in animals with mutations in *dyn-1/dynamin*, *unc-26/synaptojanin 1*, and *unc-57/endophilin* A. Our cell biological studies, both *in vivo* and by immuno-EM, support the hypothesis that in *unc-26* mutants, ATG-9 predominantly accumulates in synaptic foci, which are also enriched in clathrin. The observation that loss-of-function mutations of *unc-13/unc-18* suppress the abnormal distribution of ATG-9 in endocytic mutants shows that such redistribution is the result of abnormal endocytic traffic after exocytosis. Consistent with these findings in *C. elegans*, in mice a robust accumulation of ATG-9 was detected in nerve terminals of a subpopulation of neurons that harbor loss-of-function mutations in the genes that encode neuronal isoforms of dynamin and synaptojanin 1. Our findings in *C. elegans* are consistent with studies in *Drosophila* neurons and vertebrate cultured cells showing functional or biochemical interactions between ATG-9 and endocytic proteins synaptojanin 1 and endophilin A (Soukup et al., 2016; Vanhauwaert et al., 2017) and with adaptor protein AP-2 (Popovic and Dikic, 2014; Imai et al., 2016) and with experiments demonstrating an accumulation of ATG-9 at the plasma membrane upon perturbation of dynamin-dependent endocytosis, as detected by fluorescence microscopy (Puri et al., 2013, 2014; Popovic and Dikic, 2014) or a cell surface biotinylation assay (this study).

The exo-endocytosis of ATG-9 is important for synaptic autophagy. In mutants that disrupt endocytosis, or in mutants that disrupt the early stage of autophagy, ATG-9 redistributes to subsynaptic foci. We hypothesize that these foci may function as intermediate sorting sites (analogous to yeast reservoirs) during autophagosome biogenesis. Therefore, disruption of endocytosis, or early stage of autophagy, would similarly result in abnormal retention of ATG-9 on these intermediate sorting sites. We also hypothesize that transport and endo-exocytosis of ATG-9-containing vesicles might help bridge the activity state of the neurons with the onset of autophagosome biogenesis. This, in turn, could help “dial” the state of macroautophagy at synapses toward the degradation of damaged synaptic components at synapses under high activity states. Disruption of ATG-9 exo-endocytosis could impair the induction of local synaptic autophagy and the clearing of damaged synaptic proteins due to increased synaptic activity, eventually leading to synaptic dysfunction.

A missense mutation in the endocytic protein synaptojanin 1 in *C. elegans* (corresponding to human R258Q associated with EOP) results in abnormal accumulation of ATG-9 in

clathrin-rich synaptic foci and in age-dependent decay of synaptic physiology and behavior. Synaptojanin 1 contains two phosphatase domains: an inositol 5-phosphatase domain, which has been associated with most of the roles of synaptojanin 1 in the endocytic trafficking of SVs, and an inositol 4-phosphate Sac1 phosphatase domain, which can also dephosphorylate (to some extent) PI3P and PI(3,5)P2, and whose precise physiological function is less understood (Cremona et al., 1999; McPherson et al., 1996; Guo et al., 1999; Pirruccello and De Camilli, 2012). The R258Q mutation, which selectively abolishes the activity of the Sac1 phosphatase domain, was shown to impair presynaptic endocytic flow, and more prominently at inhibitory synapses, which have generally higher tonic activity (Cao et al., 2017), and also impair autophagy (Vanhauwaert et al., 2017). Our findings are consistent with an impact of the EOP mutation on autophagy, as we demonstrate that ATG-9 is mislocalized at synapses both in *C. elegans* harboring the homologous *unc-26(R216Q)* lesion and in the R258Q mutant mice. In *Drosophila*, the corresponding EOP mutation in synaptojanin also resulted in neurodegeneration (Vanhauwaert etal., 2017). Together, our findings support a model whereby lesions in endocytic genes associated with EOP, such as *unc-26(R216Q)*, might result in behavioral phenotypes due to their importance in sustaining the physiological functions of neurons, in part via their regulation of ATG-9 exo-endocytosis and synaptic autophagy. In view of the role of autophagy in the control of nerve terminal health and homeostasis, the defect in autophagy may then contribute to neurological deficits leading to EOP.

In conclusion, our data now support a model whereby ATG-9 couples the synaptic exo-endocytosis to autophagy (Figure 8) and thus link synaptic autophagy to the activity state of the neuron.

STAR★METHODS

RESOURCE AVAILABILITY

Lead contact—Further information and requests for resources and reagents should be directed to and will be fulfilled by the lead contact, Daniel A. Colón-Ramos (daniel.colon-ramos@yale.edu).

Materials availability—All reagents generated in this study are available from the lead contact without restriction.

Data and code availability

- Microscopy and biochemical data reported in this paper will be shared by the lead contact upon request.
- The code that quantifies expressivity of ATG-9::GFP subsynaptic foci at the presynaptic region has been deposited at GitHub and is publicly available as of the date of publication. DOIs are listed in the STAR Methods.
- Any additional information required to reanalyze the data reported in this work is available from the lead contact upon request.

EXPERIMENTAL MODEL AND SUBJECT DETAILS

***C. elegans* Strains and Genetics—**Worms were raised on nematode growth media plates at 20°C or room temperature using OP50 *Escherichia coli* as a food source (Brenner, 1974). Animals were analyzed as larva 4 (L4) stage hermaphrodites. For wild-type nematodes, *C. elegans* Bristol strain N2 was used. For a full list of strains used in the study, please see the key resources table.

Molecular Biology and Transgenic Lines—*C. elegans* transgenic strains were created by injecting pSM vector-derived plasmids (listed on key resources table) by standard injection techniques with co-injection markers punc-122::gfp and punc-122:rfp.

The cDNA constructs (UNC-26, TGN-38, Clathrin heavy chain (CHC-1)) generated were amplified from a cDNA pool of a mixed population of *C. elegans*. Detailed sub-cloning information is available upon request.

METHOD DETAILS

***C. elegans* CRISPR Transgenics—**To introduce the lesion in unc-26/synaptojanin 1 associated with early-onset Parkinsonism (EOP), we used CRISPR-Cas9 to substitute CGA with CAA, and generate the homozygous mutation R216Q. CRISPR transgenic strain was generated by precision genome editing method using CRISPR-Cas9 and linear repair templates, as previously described (Paix et al., 2017) and using the targeted gene crRNA (GGCACUCGAUUCAACGUAC) and repair template ssODN (GACGTGTTGCTCTAATATCTCGTCTAAGTTGTGAGCGTGTCGGCACTCGATTCAA CGTACAAGGAGCCAATTATCTCGGAAATGTGGCTAATTTCGTCGAGACTGAGCAAT TGTTGCTTTT)

The deletion of the ATG-9 N-terminal sorting motif (YQQID) was ordered from InVivo Biosystems *C. elegans* transgenic service.

Cell Autonomy and Rescue of *unc-26*—The *unc-26* mutant phenotype was rescued by cell specifically expressing the wild type *unc-26* cDNA under AIY-specific *ttx-3* promoter G fragment (Hobert et al., 1997).

Fluorescence Microscopy and Confocal Imaging—We imaged *C. elegans* by using 60x CFI Plan Apo VC, NA 1.4, oil objectives on an UltraView VoX spinning disc confocal microscope and on a NikonTi-E stand (PerkinElmer) with a Hammamatsu C9100–50 camera. *C. elegans* were immobilized on a 2% agarose pad with 10mM levamisole (Sigma). Images were processed with Volocity software or Fiji.

Inhibiting Oxidative Phosphorylation Using a microfluidic-hydrogel device —To inhibit oxidative phosphorylation by hypoxia, a reusable microfluidic polydimethylsiloxane (PDMS) microfluidic device was used, as described (Jang et al., 2021) while imaging ATG-9::GFP localization in *pfk-1.1(gk922689);olaIs34* or *pfk-1.1(gk922689);unc-13(s69);olaIs34* (pttx-3::atg-9::gfp and pttx-3::mCherry::rab-3). Normoxic and hypoxic conditions were applied to animals for 10 min sequentially by

alternating the flow of air and nitrogen gas, respectively. As a positive control, synaptic vesicle protein RAB-3 was also imaged as reported (Jang et al., 2016; Figures 2L and S3K).

Visualization of Different Synaptic Regions for Detecting Distinct Phenotypes—Different synaptic Zones of AIY have distinct synaptic morphologies, as reported in our ultrastructural characterizations (Figure S1) and original connectomic studies (White et al., 1986). We used these morphologies to better detect specific mutant phenotypes. For example, to observe ATG-9 accumulation into subsynaptic foci, we focused on Zone 2 of AIY, which has a relatively large, continuous presynaptic region and clearly shows changes in subsynaptic localization which are more difficult to detect in synaptic regions that are punctate to begin with. To observe the transient hypoxia-induced ATG-9 relocalization in *pfk-1.1(gk922689)* mutants, *pfk-1.1(gk922689);unc-13(s69)* double mutants, or other endocytic mutants, we focused on ATG-9 presynaptic clusters at Zone 3, which enables for us to better inspect the accumulation of the ATG-9 at the plasma membrane, a phenotype that would be harder to detect in the Zone 2 region, where ATG-9, due to the size of the presynaptic area, is localized in a distributed way in wild type animals.

ATG-9 Mislocalization Phenotypes in Response to the AIY Activity-state—To test ATG-9 mislocalization phenotypes, integrated transgenic line *olaIs34* in different genotypes was cultured at 20°C or 25°C. For the HisCl experiments, animals expressing extrachromosomal array *olaEx3465* (Pmod-1::HisCl) were cultured at 15°C and used. They were later transferred to either 10mM histamine-containing or control NGM plates at 25°C for 24 hours prior to examination. Mounting of the animals was performed as previously described (Hill et al., 2019). For the NpHR experiments, animals expressing *xuIs230* (Pttx-3s::NpHR::YFP, Pttx-3s::DsRed) (Li et al., 2014) were placed in NGM plates containing 0.4mM ATR (prepared as previously described [Collins et al., 2016]) or control plates without ATR. Green light (~560nm, ~0.2mW/mm^2) was delivered from a Leica DM500B compound fluorescent microscope to the worms for 6 hours prior to examination (Figure 3).

Electron Microscopy

High Pressure Freeze: Worms were prepared by high pressure freeze and freeze substitution as described (Rostaing et al., 2004; Manning and Richmond, 2015). Worms at the L4 stage were loaded into carriers (Specimen carrier Type A and B, Technotrade International) filled with *E. coli* and high-pressure frozen using a Leica EM HPM100.

Freeze Substitution, Morphology: After high pressure freezing, samples were transferred to an automated freeze substitution unit (Leica EM AFS2). Samples were processed in the following solutions inside the AFS: 0.1% tannic acid and 0.5% glutaraldehyde in acetone at −90°C for 98 hours, washed three times with acetone over 2 hours, 2% osmium tetroxide in acetone [−90°C for 7 hours, −90°C to −20°C over 14 hours, hold at −20°C for 16 hours, −20C to 4°C over 2.5 hours], washed four times with acetone over 3 hours, then moved to a fume hood to warm to room temperature over an hour. Sample carriers were transferred to Eppendorf tubes and infiltrated with a graded series (50/90/100%) of Epon812 in acetone over 28 hours on a rotator. Worms were dissociated from specimen carriers and surrounding

E. coli using fine needles. Two-step flat embedding was performed as described in Kolotuev (2014). Samples were cured at 60°C for two days.

Freeze Substitution, Immuno: Samples were processed in the following solutions inside the AFS: 0.1% uranyl acetate in acetone at −90°C for 48 hours, −90°C to −50°C over 8 hours, −50°C for 12 hours, washed three times with ethanol over 2 hours, infiltrated with a graded series (25/50/ 75%) of HM20 in ethanol over 22 hours, then pure HM20 for 9 hours. Two-step flat embedding was performed as described in Kolotuev (2014) in the AFS at −50°C using forceps. HM20 was polymerized under UV light at −50°C for 48 hours, −50°C to 20°C for 14 hours, 20°C for 24 hours.

Sectioning: Fixed worms were cut from the embedded square and mounted onto thin plastic blocks made using Epon resin in a Chang mold (EMS). Worms were trimmed (Diatome Trim 45) and sectioned (Diatome Ultra 45°) on a Leica UC7 (Leica) until the desired area was identified. Thick sections (500nm) were collected and stained with toluidine blue to check for the desired ROI.

The nerve ring and the AIY Zone 2 were identified using anatomical landmarks described in the original *C. elegans* connectome (White et al., 1986). The nerve ring is located in the head of the animal and forms a ring of densely packed neurites around the pharynx. AIY Zone 2 synapses are positioned in a ventral bundle of neurites just posterior to the nerve ring. These synapses reside at the ventral base of the neurite bundle and form a unique humped shape with multiple dense projections. The left and right process of AIY contact one another at the posterior end of Zone 2 synapses. Chemical synapses in *C. elegans* are defined by the presence of presynaptic dense projection in the neurite. For the morphology sections, 40nm serial sections were collected on copper slot grids covered with Formvar (EMS). Reconstructions ranged 5–15um of tissue. Grids were post stained with 2.5% uranyl acetate for 4 minutes and Reynold's lead citrate for 2 minutes.

For Immuno-EM, sections of 50nm were collected on nickel slot grids covered with Formvar (EMS). Grids were incubated at 20°C on droplets of: 0.15% glycine and 0.1M ammonium chloride in PBS for 10min, 1% BSA and 1% CWFS gelatin in PBS for 10min, anti-GFP rabbit polyclonal (1:20 in 0.3% BSA and 0.3% CWFS gelatin in PBS, ab6556 Abcam) overnight at 4°C and then 60min at 20°C, four PBS washes over 15min, Protein A Gold conjugated to 10nm gold (1:75 in 0.3% BSA and 0.3% CWFS gelatin in PBS, University Medical Center Utrecht) for 30min, four PBS washes over 15min, 1% glutaraldehyde in PBS for 5min, three water washes for 10sec. After drying, grids were post stained in 2.5% uranyl acetate for 4 minutes, and lead citrate for 1minute.

Images were acquired on a FEI Tecnai Biotwin (FEI) equipped with a SIS Morada 11 megapixel CCD camera and a TALOS L120 (Thermo Fisher) equipped with a Ceta 4k × 4k CMOS camera. For serial sections, images were aligned in z using the TrakEM2 plugin in FIJI (Cardona et al., 2012).

Imaging for Calcium Dynamics—Training and imaging for calcium dynamics for assaying AIY activity levels were performed as previously described (Hawk et al., 2018; Figure S4).

Electrophysiology—Adult hermaphrodite *C. elegans* were dissected as previously described (Richmond et al., 1999; Dong et al., 2015). Animals were immobilized on Sylgard-coated coverslips using tissue adhesive glue (Histoacryl Blue, Braun), and were dissected in extracellular solution via a dorsolateral incision using a sharpened tungsten needle. After removing gonad and intestines by suction through a glass pipette, the cuticle flap was turned and gently glued down to expose the underlying ventral nerve cord and body-wall-muscle quadrants. The worm prep was then mounted onto a fixed-stage upright microscope (BX51WI, Olympus) equipped with a 60x water-immersion objective lens. The integrity of the anterior ventral body wall muscle and the ventral nerve cord were visually examined via the DIC microscopy, and ventral muscle cells were patched using fire-polished 2–5 MΩ resistant borosilicate pipettes (World Precision Instruments, USA). Whole-cell patch clamp recordings were carried out at 20°C. Body-wall muscle cells were voltage clamped at −60 mV to record postsynaptic currents. The currents were recorded in the whole-cell configuration from muscle cells using an amplifier (EPC-10; HEKA, Germany). Extracellular solution contained (in mM) 150 NaCl, 5 KCl, 1 $CaCl_2$, 5 $MgCl_2$, 10 glucose and 10 HEPES, titrated to pH 7.3 with NaOH, 330 mOsm with sucrose. Internal solution contained 135 CH3O3SCs, 5 CsCl, 5 $MgCl_2$, 5 EGTA, 0.25 $CaCl_2$, 10 HEPES and 5 Na2ATP, adjusted to pH 7.2 using CsOH. Evoked EPSC responses were induced by applying a 0.4 ms, 30 mA pulse, generated by a stimulus isolator (A365, WPI), through a borosilicate pipette (~2 MΩ) placed in close apposition to the ventral nerve cord. Series resistance was compensated to 70% for the evoked EPSC recording. All chemicals were purchased from Sigma. Data were sampled at 10 kHz using Patchmaster (HEKA), following low-pass filtering at 2 kHz. The number of animals for each experiment was specified in Figure legends (Figures 7N, 7O, and S8K–S8N).

Worm Tracking and Locomotion Analysis—Adult animals (day 1 or day 7) were picked to 10 cm agar plates with no bacterial lawn (20 worms per plate). Imaging began 1 hour after worms were transferred. Worm crawling on the agar surface was recorded for 30 seconds using the WormLab Imaging System (MBF Bioscience, VT, USA). The center of mass was determined for each animal using custom object-tracking software developed using ImageJ (Schneider et al., 2012). Average speed was determined for each animal (Figure 7P).

Hippocampal Neuron Culture—Mice were maintained on the C57BL6/129 hybrid genetic background. Heterozygous mice were mated to generate homozygous knockout or knock-in with their littermate controls. For neuronal cultures, P0 pups were genotyped by PCR and then hippocampi were dissected. Tissues were digested for 20 min in a papain/HBSS solution (20 U/ml) containing DNase (20 μg/ml). Cells were dissociated by trituration and then plated onto poly-d-lysine coated coverslips. After 3 hours incubation, the plating medium was exchanged to complete neurobasal medium (2% B-27 and 0.5 mM L-glutamine in neurobasal medium). Cells were maintained at 37°C in a 5% CO_2 humidified incubator

and the 30% of cultured medium was replaced with new complete neurobasal medium at 4, 7 and 14 days in vitro (DIV). All adult mice for breeding were maintained on a 12 hours light/dark cycle with standard mouse chow and water ad libitum. The general protocol used for hippocampal neuron culture was deposited in protocols.io: https://dx.doi.org/10.17504/protocols.io.b2deqa3e. All research and animal care procedures were approved by the Yale University Institutional Animal Care and Use Committee.

Immunofluorescence—Cultured hippocampal neurons were briefly washed in a pre-warmed tyrode (136 mM NaCl, 2.5 mM KCl, 2 mM $CaCl_2$, 1.3 mM $MgCl_2$, 10 mM HEPES and 10 mM glucose) and then fixed with 4% PFA in 4% sucrose-containing 0.1M PB buffer (pH7.3) for 15 min at RT. After fixation, cells were washed in PBS and incubated with blocking buffer (3% BSA, 0.2% Triton X-100 in PBS) for 30 min at RT. Primary (1 hour) and secondary antibody (45 min) incubations were subsequently performed in the blocking buffer at room temperature. After washing, samples were mounted on slides with Prolong Gold antifade reagent (Invitrogen). The detailed protocol used for immunofluorescence was deposited in protocols.io: https://dx.doi.org/10.17504/protocols.io.b2c7qazn.

Dynamin Conditional Knockout—For the tamoxifen inducible KO, Dynamin 1/2 conditional knockout (CKO) cells (Ferguson et al., 2009) were treated with 2 μM 4-hydroxy-tamoxifen for 2 days and then further incubated with 300 nM 4-hydroxy-tamoxifen for 3 days. Depletion of total dynamin levels was confirmed by western blotting. The detailed protocol used for dynamin conditional knockout was deposited in protocols.io: https://dx.doi.org/10.17504/protocols.io.b2ddqa26.

Surface Protein Biotinylation—Control and dynamin 1/2 conditional KO cells were washed three times with ice-cold PBS and incubated with ice-cold EZ-Link Sulfo-NHS-LC-Biotin (0.25 mg/ml) in PBS for 30 min at 4 °C to label the surface proteins. Unbound biotins were quenched and removed by 50 mM glycine in ice-cold PBS for 10 min at 4 °C. After washout, cells were lysed with 1% triton X-100 lysis buffer (20 mM Tris-HCl, pH 8, 1% triton X-100, 10% glycerol, 137 mM NaCl, 2 mM EDTA, 1 mM PMSF, 10 mM leupeptin, 1.5 mM pepstatin and 1 mM aprotinin) and centrifuged at 14,000 g for 20 min at 4°C. The supernatants were collected, and protein concentrations were determined by the BCA Protein Assay Kit. Same amount of lysates (600 μg) were incubated with NeutraAvidin particles for 2 hours at 4 °C to pull-down the biotinylated proteins. Particles were washed three times by lysis buffer, eluted with 2x sample buffer and boiling (5 min) and the eluates were processed for SDS-PAGE and western blotting. The level of proteins was quantified by densitometry using Fiji. The detailed protocol used for surface protein biotinylation was deposited in protocols.io: https://doi.org/10.17504/protocols.io.b2c8qazw.

QUANTIFICATION AND STATISTICAL ANALYSIS

C. elegans AIY Quantifications

Presynaptic Enrichment: Morphologically, AIY can be divided into four segments, consistent with the *C. elegans* EM reconstructions and our own ultrastructural studies (White et al., 1986; Figure S1): the cell body; a proximal asynaptic region termed Zone 1; a ~5mm

synaptic-rich region termed Zone 2, located at the turn of the neuron into the nerve ring; and Zone 3, which is the distal part of the neurite located at the nerve ring.

ATG-9 or RAB-3 enrichment at synapses was quantified in the integrated transgenic line *olaIs34*, expressing pttx-3::atg-9::gfp and pttx-3::mCherry::rab-3 in the wild type and *apb-3(ok429)* mutants. Fluorescence intensity at Zone 2 was quantified in Fiji (Schindelin et al., 2012) in maximal projection confocal micrographs. ATG-9 (or RAB-3) enrichment at synapses represents Zone 2 signal subtracted by average cytoplasmic signal at the cell body (Figures 1X and S2M).

Ratio of ATG-9 intensity of cell body/synapses was quantified in *olaIs34* in the wild type, *apb-3(ok429)*, *apm-3(gk771233)* and *apd-3(gk805642)* mutants. In maximal projection confocal micrographs, fluorescence intensities were measured, background-subtracted (from cytoplasmic signal at the cell body) and averaged for different subcellular regions (using an identically-sized oval-shaped object). The 'Ratio between ATG-9 intensity at the cell body and synapses' represents signal of ATG-9 intensity (after the processing) at the cell body divided by the intensity (after the processing) at Zone 2 (as shown in the equation below; Figures 1Y and S2Q).

$$The\ ratio = \frac{ATG-9\ intensity\ at\ cell\ body - cytoplasmic\ background}{ATG-9\ intensity\ at\ zone\ 2 - cytoplasmic\ background}$$

To quantify ratio of SNG-1 intensity of cell body/synapses, we used the extrachromosomal line *olaex4060* in the wild type and *apb-3(ok429)* mutants. Maximal projection confocal micrographs were taken on SNG-1 and measured as the intensity at Zone 2 by segmented line scans and the intensity at the cell body by the oval selections of the whole cell body. The ratio of SNG-1 intensity between cell body and synapses was reported as the intensity of SNG-1 at cell body divided by the intensity of SNG-1 at Zone 2 (Figure 1Z).

Penetrance of ATG-9::GFP Subsynaptic Foci at the Presynaptic Region: To quantify the penetrance of ATG-9 subsynaptic foci at the presynaptic region (Zone 2), we used integrated transgenic strain *olaIs34* and *olaIs33* in the wild type and mutant background animals. For the temperature sensitive allele *dyn-1(ky51)* and the wild-type animals, animals were held at either 20°C (permissive) or 25°C (non-permissive) for 3 days (or longer) prior to examination at the L4 stage. Other mutants were kept at 20°C except for *unc-26(s1710)* and *epg-9(bp320)* temperature experiments.

The penetrance of ATG-9 subsynaptic foci was quantified as percentage of animals showing subsynaptic foci of ATG-9::GFP at Zone 2. Mutant phenotype was defined as two or more than two subsynaptic foci of ATG-9::GFP at Zone 2 in endocytic mutants, or one or more than one subsynaptic foci in autophagy mutants, as the penetrance and expressivity of the phenotype in autophagy mutants are lower than the endocytic mutants. A Leica DM500B compound fluorescent microscope was used to visualize and screen the worm in different genetic backgrounds (Figures 3E, 5G, 5H, 5L, S3A, S8B, S8C, and S8J).

Expressivity of ATG-9::GFP Subsynaptic Foci at the Presynaptic Region: To quantify expressivity of ATG-9 subsynaptic foci at the presynaptic region (Zone 2), we obtained the plot profiles for individual presynaptic region (Zone 2) through segmented line scans using Fiji. A MATLAB function, *findpeaks*, was used to identify peaks along the line scans of Zone 2. The index of ATG-9 mislocalization at presynaptic region is defined as the number of peaks divided by the width of peaks at Zone 2 in each individual animal. In endocytic mutants, two populations of mutant phenotype were identified: ATG-9 is dim at Zone 2; ATG-9 displays subsynaptic foci at Zone 2. A threshold in the algorithm was used to eliminate worms that have ATG-9 dim signals (Figure 2K).

Code is available here in GitHub: https://github.com/yangsisi76/Quantify-distribution-of-cell-structures.

Mean Intensity of ATG-9 at Zone 2: To measure the level of ATG-9 at presynaptic regions, we obtained the fluorescent value for individual presynaptic region (Zone 2) through segmented line scans using Fiji. All settings for the confocal microscope and camera were kept identical between the wild type and *unc-26(s1710)* mutants. Mean fluorescent value of animals in the two genotypes was calculated by Fiji (Figure S3B).

RAB-3 and SNG-1 Enrichment at Zone 3: To quantify the distribution and enrichment of synaptic proteins, such as RAB-3 and SNG-1, we used methods as described (Dittman and Kaplan, 2006; Jang et al., 2016). Briefly, fluorescent values for the RAB-3 (SNG-1) in AIY neurons were obtained through segmented line scans using Fiji. A sliding window of 2mm was used to identify all the fluorescent peak and trough values for Zone 3 in each individual neuron. The synaptic enrichment was calculated as $\%\Delta F/F$ as described (Jang et al., 2016; Dittman and Kaplan, 2006; Bai et al., 2010). In short, all the identified fluorescent peak and trough values (F_{peak} and F_{trough}) were averaged and used to calculate the $\%\Delta F/F$ ($100 \times (F_{peak} - F_{trough})/ F_{trough}$) (Bai et al., 2010; Dittman and Kaplan, 2006; Jang et al., 2016). All settings for the confocal microscope and camera were kept identical between the wild type and *unc-26(s1710)* mutants (Figures S5L and S8I).

Percentage of ATG-9 Subsynaptic Foci that Colocalize with the Subsynaptic Structures and Pearson's R Value between ATG-9 and Organelles: To quantify the percentage of ATG-9 subsynaptic foci that colocalize with the subsynaptic structures (LGG-1 and CHC-1), we observed the transgenic lines *olaex1360;olaIs44* (pttx-3::gfp::lgg-1, pttx-3::mCherry::atg-9) and *olaex4290;olaIs34* (pttx-3::bfp::chc-1, pttx-3::atg-9::gfp). Confocal maximal projections were used, and percentage colocalization was calculated as the percentage of ATG-9 subsynaptic foci that colocalize with examined, discrete organelle marker (Figure 4L).

To quantify the Pearson's R value between ATG-9 and organelles at cell body, we observed transgenic lines *olaEx4710* (pttx-3::aman-2::gfp, pttx-3::atg-9::mCh), *olaEx4966* (pttx-3::atg-9::gfp, pttx-3::tgn-38::mCh), *olaEx4805* (pttx-3::sp12::GFP, pttx-3::atg-9::mCh) and *olaEx5178* (pttx-3::tomm-20::gfp, pttx-3::atg-9::mCh). Confocal maximal projections were used, and Pearson's R value (no threshold) was calculated between two channels (Figure S2H).

Activity-induced Autophagy: To measure the synaptic autophagosomes in AIY, animals with *olaIs35* in the wild-type, *unc-13(e450)*, *atg-9(wy56)*, *unc-26(s1710)*, *unc-26(s1710);atg-9(wy56)* and *atg-9(*D*AP)* mutant backgrounds were grown in 20°C and then shifted to 25°C for 4 hours and assessed for number of LGG-1 puncta in the neurite of AIY under a Leica DM 5000B compound microscope (Hill et al., 2019; Figures 5M and S7D–S7G).

Immuno-EM: To quantify the distribution of ATG-9 positive particles, animals with *olaex2264* (punc-14::atg-9::gfp) in the wild type and *unc-26(e205)* mutants were used. Quantifications were performed in FIJI. Cross-sectional area: an image of a 40nm section. Particles were counted using the Cell Counter plugin. Occasionally, a Gaussian Blur processing filter was applied in FIJI to help visualize structures in the image. Staining specificity, calculated as a signal to noise ratio of particle density in neuronal tissue divided by particle density in nearby *E. coli* in the section, was >20 for all samples. Particles were considered localized near vesicles, plasma membrane, or mitochondria if the distance from the gold particle to that structure was <20 nm. This distance was chosen based on estimates of the size of GFP, a GFP antibody, and protein A crystal structures. To measure the area occupied by vesicles, a freehand shape was drawn around an apparent cluster of vesicles occupying most or all vesicles in the neurite. To measure area occupied by plasma membrane, the perimeter of the neurite was multiplied by 40, which accounts for the rough measured width of the plasma membrane plus the 20 nm radius in which a particle may be localized nearby (Figures 1G, 4A, 4B, and S1G–S1J).

Zone 2 Morphological EM: For each image of a single 40 nm section, or profile, we segmented plasma membrane, dense projections, active zones, vesicles and mitochondria. Active zones were defined as continuous length plasma membrane in a single cross section that flank the dense projection, extending to the beginning of the closest adherens junction. Data were analyzed as per profile or per synapse. A synapse is defined as reconstructed set of profiles that span a dense projection. Zone 2 is a giant synapse that contains multiple active zones, defined by multiple dense projections (Figures S1A–S1F and S6).

Quantification of Immunoreactivity in Hippocampal Neuron Culture and GFP::CHC-1 in *C. elegans*—Quantification of ATG9 and CHC-1 clustering was performed using Fiji as previously described (Cao et al., 2020). Briefly, the same threshold was applied to all images after background subtraction and then ‘analyze particles’ function of Fiji was used to obtain the raw intensity values of masked regions (Figures S5H and S8A).

QUANTIFICATION, STATISTICAL ANALYSIS AND MODELS

Statistical analysis and data plotting were conducted with Prism 9 software. We used Fisher’s exact test to determine statistical significance of categorical data in contingency table, such as the penetrance of ATG-9 phenotype in AIY. 95% confidence intervals were calculated by Wilson/Brown method and used for error bars. Each dot in the scatter plots or n represents number of animals or ATG-9 subsynaptic structures examined. For the continuous data, ordinary one-way ANOVA with Tukey’s multiple comparisons test and

with Tukey's HSD post hoc test, Welch's t test, Student's t test and paired t test were used to determine its statistical significance. Each dot in the scatter plots or n represents number of animals, sections in immuno-EM or independent experiments examined. The error bars represent the standard error of the mean (SEM). The p value for significant differences is reported in the figure legends.

The model and graphic abstract are adapted from "Neuronal Cells" and "Organelles", by BioRender.com (2021). Retrieved from https://app.biorender.com/biorender-templates.

Supplementary Material

Refer to Web version on PubMed Central for supplementary material.

ACKNOWLEDGMENTS

We thank Erik Jorgensen (Department of Biology, University of Utah), Kang Shen (Department of Biology, Stanford University), and Hong Zhang (Institute of Biophysics, Chinese Academy of Sciences) for providing strains and constructs. We thank the Center for Cellular and Molecular Imaging, Electron Microscopy Facility at Yale Medical School for assistance with the work presented here, and Yumei Wu, Irina Kolotuev, David Hall, Maike Kittelmann, and Szi-chieh Yu for advice on immunoelectron microscopy experiments. We thank Shawn Xu for providing strain TQ3509. We thank Elias M. Wisdom for performing exploratory experiments on locomotory behavior. We thank current and past members of the Colón-Ramos Lab for help, advice, and insightful comments on the project. We thank the Caenorhabditis Genetics Center (funded by NIH Office of Research Infrastructure Programs P40 OD010440) for *C. elegans* strains. S.Y. was supported by the China Scholarship Council-Yale World Scholars Program. I.O.'s summer research was supported by Howard Hughes Medical Institute Exceptional Research Opportunities Program (HHMI ExROP) and Yale BioMed Amgen Scholars Program. Research in the J.B. lab was supported by the NIH (NS115974, GM127857, and NS109476). Research in the P.D.C. lab was supported in part by the NIH (NS36251, DA18343, and DK45735), the Parkinson Foundation (United States), the Kavli Foundation, and by Aligning Science Across Parkinson's (ASAP)-000580 through the Michael J. Fox Foundation for Parkinson's Research (MJFF), and D.P. was supported in part by a fellowship from the National Research Foundation of Korea (2019R1A6A3A03031300). Research in the D.A.C.-R. lab was supported by NIH R01NS076558, DP1NS111778, and by an HHMI Scholar Award. For the purpose of open access, the authors have applied a CC-BY public copyright license to the author accepted manuscript (AAM) version arising from this submission.

REFERENCES

Alberti A, Michelet X, Djeddi A, and Legouis R. (2010). The autophagosomal protein LGG-2 acts synergistically with LGG-1 in dauer formation and longevity in C. elegans. Autophagy 6, 622–633. [PubMed: 20523114]

Alegre-Abarrategui J, and Wade-Martins R. (2009). Parkinson disease, LRRK2 and the endocytic-autophagic pathway. Autophagy 5, 1208–1210. [PubMed: 19770575]

Altun-Gultekin Z, Andachi Y, Tsalik EL, Pilgrim D, Kohara Y, and Hobert O. (2001). A regulatory cascade of three homeobox genes, ceh-10 ttx-3 and ceh-23, controls cell fate specification of a defined interneuron class in C. elegans. Development 128, 1951–1969. [PubMed: 11493519]

Andres-Alonso M, Kreutz MR, and Karpova A. (2021). Autophagy and the endolysosomal system in presynaptic function. Cell. Mol. Life Sci. 78, 2621–2639. [PubMed: 33340068]

Azarnia Tehran D, Kuijpers M, and Haucke V. (2018). Presynaptic endocytic factors in autophagy and neurodegeneration. Curr. Opin. Neurobiol. 48, 153–159. [PubMed: 29316491]

Bai JH, Hu ZT, Dittman JS, Pym ECG, and Kaplan JM (2010). Endophilin functions as a membrane-bending molecule and is delivered to endocytic zones by exocytosis. Cell 143, 430–441. [PubMed: 21029864]

Bandres-Ciga S, Saez-Atienzar S, Bonet-Ponce L, Billingsley K, Vitale D, Blauwendraat C, Gibbs JR, Pihlstrøm L, Gan-Or Z, et al. ; International Parkinson's Disease Genomics Consortium (IPDGC) (2019). The endocytic membrane trafficking pathway plays a major role in the risk of Parkinson's disease. Mov. Disord. 34, 460–468. [PubMed: 30675927]

Behne R, Teinert J, Wimmer M, D'Amore A, Davies AK, Scarrott JM, Eberhardt K, Brechmann B, Chen IP, Buttermore ED, et al. (2020). Adaptor protein complex 4 deficiency: a paradigm of childhood-onset hereditary spastic paraplegia caused by defective protein trafficking. Hum. Mol. Genet. 29, 320–334. [PubMed: 31915823]

Binotti B, Pavlos NJ, Riedel D, Wenzel D, Vorbrüggen G, Schalk AM, Kühnel K, Boyken J, Erck C, Martens H, et al. (2015). The GTPase Rab26 links synaptic vesicles to the autophagy pathway. Elife 4, e05597.

Blauwendraat C, Heilbron K, Vallerga CL, Bandres-Ciga S, von Coelln R, Pihlstrøm L, Simón-Sánchez J, Schulte C, Sharma M, Krohn L, et al. (2019). Parkinson's disease age at onset genome-wide association study: defining heritability, genetic loci, and alpha-synuclein mechanisms. Mov. Disord. 34, 866–875. [PubMed: 30957308]

Boyken J, Grønborg M, Riedel D, Urlaub H, Jahn R, and Chua JJE (2013). Molecular profiling of synaptic vesicle docking sites reveals novel proteins but few differences between glutamatergic and GABAergic synapses. Neuron 78, 285–297. [PubMed: 23622064]

Brenner S. (1974). The genetics of Caenorhabditis elegans. Genetics 77, 71–94. [PubMed: 4366476]

Bunge MB (1973). Fine structure of nerve fibers and growth cones of isolated sympathetic neurons in culture. J. Cell Biol. 56, 713–735. [PubMed: 4347207]

Cao M, Wu Y, Ashrafi G, Mccartney AJ, Wheeler H, Bushong EA, Boassa D, Ellisman MH, Ryan TA, and De Camilli P. (2017). Parkinson sac domain mutation in synaptojanin 1 impairs clathrin uncoating at synapses and triggers dystrophic changes in dopaminergic axons. Neuron 93, 882–896.e5. [PubMed: 28231468]

Cao MA, Park D, Wu YM, and De Camilli P. (2020). Absence of Sac2/ INPP5F enhances the phenotype of a Parkinson's disease mutation of synaptojanin 1. Proc. Natl. Acad. Sci. USA 117, 12428–12434.

Cardona A, Saalfeld S, Schindelin J, Arganda-Carreras I, Preibisch S, Longair M, Tomancak P, Hartenstein V, and Douglas RJ (2012). TrakEM2 software for neural circuit reconstruction. PLoS One 7, e38011.

Chantranupong L, Saulnier JL, Wang W, Jones DR, Pacold ME, and Sabatini BL (2020). Rapid purification and metabolomic profiling of synaptic vesicles from mammalian brain. Elife 9, e59699.

Cheung ZH, and Ip NY (2009). The emerging role of autophagy in Parkinson's disease. Mol. Brain 2, 29. [PubMed: 19754977]

Collins KM, Bode A, Fernandez RW, Tanis JE, Brewer JC, Creamer MS, and Koelle MR (2016). Activity of the C. elegans egg-laying behavior circuit is controlled by competing activation and feedback inhibition. Elife 5, e21126.

Colón-Ramos DA, Margeta MA, and Shen K. (2007). Glia promote local synaptogenesis through UNC-6 (netrin) signaling in C. elegans. Science 318, 103–106. [PubMed: 17916735]

Cowles CR, Odorizzi G, Payne GS, and Emr SD (1997). The AP-3 adaptor complex is essential for cargo-selective transport to the yeast vacuole. Cell 91, 109–118. [PubMed: 9335339]

Crawley O, Opperman KJ, Desbois M, Adrados I, Borgen MA, Giles AC, Duckett DR, and Grill B. (2019). Autophagy is inhibited by ubiquitin ligase activity in the nervous system. Nat. Commun. 10, 5017. [PubMed: 31676756]

Cremona O, Di Paolo G, Wenk MR, Lüthi A, Kim WT, Takei K, Daniell L, Nemoto Y, Shears SB, Flavell RA, et al. (1999). Essential role of phosphoinositide metabolism in synaptic vesicle recycling. Cell 99, 179–188. [PubMed: 10535736]

De Pace R, Skirzewski M, Damme M, Mattera R, Mercurio J, Foster AM, Cuitino L, Jarnik M, Hoffmann V, Morris HD, et al. (2018). Altered distribution of ATG9A and accumulation of axonal aggregates in neurons from a mouse model of AP-4 deficiency syndrome. PLoS Genet. 14, e1007363.

Dell'Angelica EC (2009). AP-3-dependent trafficking and disease: the first decade. Curr. Opin. Cell Biol. 21, 552–559. [PubMed: 19497727]

Dittman JS, and Kaplan JM (2006). Factors regulating the abundance and localization of synaptobrevin in the plasma membrane. Proc. Natl. Acad. Sci. USA 103, 11399–11404.

Dong YM, Gou YY, Li Y, Liu Y, and Bai JH (2015). Synaptojanin coop- erates in vivo with endophilin through an unexpected mechanism. Elife 4, e05660.

Ebrahimi-Fakhari D, Behne R, Davies AK, and Hirst J. (1993). AP-4-associated hereditary spastic paraplegia. In GeneReviews®, Adam MP, Ardinger HH, Pagon RA, Wallace SE, Bean LJH, Mirzaa G, and Amemiya A, eds. (University of Washington).

Feng YC, and Klionsky DJ (2017). Autophagic membrane delivery through ATG9. Cell Res 27, 161–162. [PubMed: 28072404]

Ferguson SM, Brasnjo G, Hayashi M, Wölfel M, Collesi C, Giovedi S, Raimondi A, Gong LW, Ariel P, Paradise S, et al. (2007). A selective ac- tivity-dependent requirement for dynamin 1 in synaptic vesicle endocytosis. Science 316, 570–574. [PubMed: 17463283]

Ferguson SM, and De Camilli P. (2012). Dynamin, a membrane-remodelling GTPase. Nat. Rev. Mol. Cell Biol. 13, 75–88. [PubMed: 22233676]

Ferguson SM, Raimondi A, Paradise S, Shen H, Mesaki K, Ferguson A, Destaing O, Ko G, Takasaki J, Cremona O, et al. (2009). Coordinated actions of actin and BAR proteins upstream of dynamin at endocytic clathrin-coated pits. Dev. Cell 17, 811–822. [PubMed: 20059951]

George AA, Hayden S, Stanton GR, and Brockerhoff SE (2016). Arf6 and the 5′phosphatase of synaptojanin 1 regulate autophagy in cone photoreceptors. BioEssays 38 (Suppl 1), S119–S135. [PubMed: 27417116]

Ghanbarpour A, Valverde DP, Melia TJ, and Reinisch KM (2021). A model for a partnership of lipid transfer proteins and scramblases in membrane expansion and organelle biogenesis. Proc. Natl. Acad. Sci. USA 118, e2101562118.

Gómez-Sánchez R, Rose J, Guimarães R, Mari M, Papinski D, Rieter E, Geerts WJ, Hardenberg R, Kraft C, Ungermann C, and Reggiori F. (2018). Atg9 establishes Atg2-dependent contact sites between the endoplasmic reticulum and phagophores. J. Cell Biol. 217, 2743–2763. [PubMed: 29848619]

Guardia CM, Christenson ET, Zhou W, Tan XF, Lian T, Faraldo-Gómez JD, Bonifacino JS, Jiang J, and Banerjee A. (2020). The structure of human ATG9A and its interplay with the lipid bilayer. Autophagy 16, 2292–2293. [PubMed: 33016201]

Guo S, Stolz LE, Lemrow SM, and York JD (1999). SAC1-like domains of yeast SAC1, INP52, and INP53 and of human synaptojanin encode poly-phosphoinositide phosphatases. J. Biol. Chem. 274, 12990–12995.

Harris TW, Hartwieg E, Horvitz HR, and Jorgensen EM (2000). Mutations in synaptojanin disrupt synaptic vesicle recycling. J. Cell Biol. 150, 589–600. [PubMed: 10931870]

Hata Y, Slaughter CA, and Südhof TC (1993). Synaptic vesicle fusion complex contains unc-18 homologue bound to syntaxin. Nature 366, 347–351. [PubMed: 8247129]

Hawk JD, Calvo AC, Liu P, Almoril-Porras A, Aljobeh A, Torruella- Suárez ML, Ren I, Cook N, Greenwood J, Luo LJ, et al. (2018). Integration of plasticity mechanisms within a single sensory neuron of C. elegans actuates a memory. Neuron 97, 356–367.e4. [PubMed: 29307713]

Hayashi M, Raimondi A, O'Toole E, Paradise S, Collesi C, Cremona O, Ferguson SM, and De Camilli P. (2008). Cell-and stimulus-dependent heterogeneity of synaptic vesicle endocytic recycling mechanisms revealed by studies of dynamin 1-null neurons. Proc. Natl. Acad. Sci. USA 105, 2175–2180. [PubMed: 18250322]

Hill SE, and Colón-Ramos DA (2020). The journey of the synaptic autophagosome: a cell biological perspective. Neuron 105, 961–973. [PubMed: 32191859]

Hill SE, Kauffman KJ, Krout M, Richmond JE, Melia TJ, and Colón-Ramos DA (2019). Maturation and clearance of autophagosomes in neurons depends on a specific cysteine protease isoform, ATG-4.2. Dev. Cell 49, 251–266.e8. [PubMed: 30880001]

Hobert O, Mori I, Yamashita Y, Honda H, Ohshima Y, Liu YX, and Ruvkun G. (1997). Regulation of interneuron function in the C. elegans thermoregulatory pathway by the ttx-3 LIM homeobox gene. Neuron 19, 345–357. [PubMed: 9292724]

Hou X, Watzlawik JO, Fiesel FC, and Springer W. (2020). Autophagy in Parkinson's disease. J. Mol. Biol. 432, 2651–2672. [PubMed: 32061929]

Huang S, Jia K, Wang Y, Zhou Z, and Levine B. (2013). Autophagy genes function in apoptotic cell corpse clearance during C. elegans embryonic development. Autophagy 9, 138–149. [PubMed: 23108454]

Imai K, Hao F, Fujita N, Tsuji Y, Oe Y, Araki Y, Hamasaki M, Noda T, and Yoshimori T. (2016). Atg9A trafficking through the recycling endosomes is required for autophagosome formation. J. Cell Sci. 129, 3781–3791. [PubMed: 27587839]

Ivankovic D, Drew J, Lesept F, White IJ, López Doménech GL, Tooze SA, and Kittler JT (2020). Axonal autophagosome maturation defect through failure of ATG9A sorting underpins pathology in AP-4 deficiency syndrome. Autophagy 16, 391–407. [PubMed: 31142229]

Jang S, Nelson JC, Bend EG, Rodríguez-Laureano L, Tueros FG, Cartagenova L, Underwood K, Jorgensen EM, and Colón-Ramos DA (2016). Glycolytic enzymes localize to synapses under energy stress to support synaptic function. Neuron 90, 278–291. [PubMed: 27068791]

Jang S, Xuan Z, Lagoy RC, Jawerth LM, Gonzalez IJ, Singh M, Prashad S, Kim HS, Patel A, Albrecht DR, et al. (2021). Phosphofructokinase relocalizes into subcellular compartments with liquid-like properties in vivo. Biophys. J. 120, 1170–1186. [PubMed: 32853565]

Karabiyik C, Lee MJ, and Rubinsztein DC (2017). Autophagy impairment in Parkinson's disease. Essays Biochem. 61, 711–720. [PubMed: 29233880]

Katsumata K, Nishiyama J, Inoue T, Mizushima N, Takeda J, and Yuzaki M. (2010). Dynein- and activity-dependent retrograde transport of autophagosomes in neuronal axons. Autophagy 6, 378–385. [PubMed: 20150763]

Kim WT, Chang SH, Daniell L, Cremona O, Di Paolo G, and De Camilli P. (2002). Delayed reentry of recycling vesicles into the fusion-competent synaptic vesicle pool in synaptojanin 1 knockout mice. Proc. Natl. Acad. Sci. USA 99, 17143–17148.

Kolotuev I. (2014). Positional correlative anatomy of invertebrate model organisms increases efficiency of TEM data production. Microsc. Microanal. 20, 1392–1403. [PubMed: 25180638]

Kononenko NL, Claßen GA, Kuijpers M, Puchkov D, Maritzen T, Tempes A, Malik AR, Skalecka A, Bera S, Jaworski J, and Haucke V. (2017). Retrograde transport of TrkB-containing autophagosomes via the adaptor AP-2 mediates neuronal complexity and prevents neurodegeneration. Nat. Commun. 8, 14819.

Krebs CE, Karkheiran S, Powell JC, Cao M, Makarov V, Darvish H, Di Paolo G, Walker RH, Shahidi GA, Buxbaum JD, et al. (2013). The Sac1 domain of SYNJ1 identified mutated in a family with early-onset progressive Parkinsonism with generalized seizures. Hum. Mutat. 34, 1200–1207. [PubMed: 23804563]

Kuijpers M, Azarnia Tehran D, Haucke V, and Soykan T. (2021). The axonal endolysosomal and autophagic systems. J. Neurochem. 158, 589–602. [PubMed: 33372296]

Kulkarni A, Chen J, and Maday S. (2018). Neuronal autophagy and intercellular regulation of homeostasis in the brain. Curr. Opin. Neurobiol. 51, 29–36. [PubMed: 29529415]

Kulkarni VV, Anand A, Herr JB, Miranda C, Vogel MC, and Maday S. (2021). Synaptic activity controls autophagic vacuole motility and function in dendrites. J. Cell Biol. 220, e202002084.

Lang T, Reiche S, Straub M, Bredschneider M, and Thumm M. (2000). Autophagy and the cvt pathway both depend on AUT9. J. Bacteriol. 182, 2125–2133. [PubMed: 10735854]

Li LB, Lei H, Arey RN, Li P, Liu J, Murphy CT, Xu XZ, and Shen K. (2016). The neuronal kinesin UNC-104/KIF1A is a key regulator of synaptic aging and insulin signaling-regulated memory. Curr. Biol. 26, 605–615. [PubMed: 26877087]

Li ZY, Liu J, Zheng MH, and Xu XZS (2014). Encoding of both analog- and digital-like behavioral outputs by one C. elegans interneuron. Cell 159, 751–765. [PubMed: 25417153]

Liang QQ, Yang PG, Tian E, Han JH, and Zhang H. (2012). The C. elegans ATG101 homolog EPG-9 directly interacts with EPG-1/Atg13 and is essential for autophagy. Autophagy 8, 1426–1433. [PubMed: 22885670]

Liang Y, and Sigrist S. (2018). Autophagy and proteostasis in the control of synapse aging and disease. Curr. Opin. Neurobiol. 48, 113–121. [PubMed: 29274917]

Lu J, Wu M, and Yue Z. (2020). Autophagy and Parkinson's disease. Adv. Exp. Med. Biol. 1207, 21–51. [PubMed: 32671737]

Lu Q, Yang P, Huang X, Hu W, Guo B, Wu F, Lin L, Kovács AL, Yu L, and Zhang H. (2011). The WD40 repeat PtdIns(3)P-binding protein EPG-6 regulates progression of omegasomes to autophagosomes. Dev. Cell 21, 343–357. [PubMed: 21802374]

Luthi A, Di Paolo G, Cremona O, Daniell L, De Camilli P, and Mccormick DA (2001). Synaptojanin 1 contributes to maintaining the stability of GABAergic transmission in primary cultures of cortical neurons. J. Neurosci. 21, 9101–9111. [PubMed: 11717343]

Lynch-Day MA, Mao K, Wang K, Zhao M, and Klionsky DJ (2012). The role of autophagy in Parkinson's disease. Cold Spring Harb. Perspect. Med. 2, a009357.

Maday S, Wallace KE, and Holzbaur EL (2012). Autophagosomes initiate distally and mature during transport toward the cell soma in primary neurons. J. Cell Biol. 196, 407–417. [PubMed: 22331844]

Maeda S, Yamamoto H, Kinch LN, Garza CM, Takahashi S, Otomo C, Grishin NV, Forli S, Mizushima N, and Otomo T. (2020). Structure, lipid scrambling activity and role in autophagosome formation of ATG9A. Nat. Struct. Mol. Biol. 27, 1194–1201. [PubMed: 33106659]

Manil-Ségalen M, Lefebvre C, Jenzer C, Trichet M, Boulogne C, Satiat-Jeunemaitre B, and Legouis R. (2014). The C. elegans LC3 acts downstream of GABARAP to degrade autophagosomes by interacting with the HOPS subunit VPS39. Dev. Cell 28, 43–55. [PubMed: 24374177]

Manning L, and Richmond J. (2015). High-pressure freeze and freeze substitution electron microscopy in C. elegans. Methods Mol. Biol. 1327, 121–140. [PubMed: 26423972]

Margeta MA, Wang GJ, and Shen K. (2009). Clathrin adaptor AP-1 complex excludes multiple postsynaptic receptors from axons in C. elegans. Proc. Natl. Acad. Sci. USA 106, 1632–1637. [PubMed: 19164532]

Matoba K, Kotani T, Tsutsumi A, Tsuji T, Mori T, Noshiro D, Sugita Y, Nomura N, Iwata S, Ohsumi Y, et al. (2020). Atg9 is a lipid scramblase that mediates autophagosomal membrane expansion. Nat. Struct. Mol. Biol. 27, 1185–1193. [PubMed: 33106658]

Matoba K, and Noda NN (2020). Secret of Atg9: lipid scramblase activity drives de novo autophagosome biogenesis. Cell Death Differ 27, 3386–3388. [PubMed: 33177618]

Mattera R, Park SY, De Pace R, Guardia CM, and Bonifacino JS (2017). AP-4 mediates export of ATG9A from the trans-Golgi network to promote autophagosome formation. Proc. Natl. Acad. Sci. USA 114, E10697– E10706.

Mcpherson PS, Garcia EP, Slepnev VI, David C, Zhang XM, Grabs D, Sossin WS, Bauerfeind R, Nemoto Y, and De Camilli P. (1996). A presyn- aptic inositol-5-phosphatase. Nature 379, 353–357. [PubMed: 8552192]

Menzies FM, Fleming A, Caricasole A, Bento CF, Andrews SP, Ashkenazi A, Füllgrabe J, Jackson A, Jimenez Sanchez M, Karabiyik C, et al. (2017). Autophagy and neurodegeneration: pathogenic mechanisms and therapeutic opportunities. Neuron 93, 1015–1034. [PubMed: 28279350]

Milosevic I, Giovedi S, Lou X, Raimondi A, Collesi C, Shen H, Paradise S, O'Toole E, Ferguson S, Cremona O, and De Camilli P. (2011). Recruitment of endophilin to clathrin-coated pit necks is required for efficient vesicle uncoating after fission. Neuron 72, 587–601. [PubMed: 22099461]

Murdoch JD, Rostosky CM, Gowrisankaran S, Arora AS, Soukup SF, Vidal R, Capece V, Freytag S, Fischer A, Verstreken P, et al. (2016). Endophilin-A deficiency induces the Foxo3a-Fbxo32 network in the brain and causes dysregulation of autophagy and the ubiquitin-proteasome system. Cell Rep 17, 1071–1086. [PubMed: 27720640]

Nakatsu F, and Ohno H. (2003). Adaptor protein complexes as the key regulators of protein sorting in the post-Golgi network. Cell Struct. Funct. 28, 419–429. [PubMed: 14745134]

Nalls MA, Pankratz N, Lill CM, Do CB, Hernandez DG, Saad M, DeStefano AL, Kara E, Bras J, Sharma M, et al. (2014). Large-scale meta-analysis of genome-wide association data identifies six new risk loci for Parkinson's disease. Nat. Genet. 46, 989–993. [PubMed: 25064009]

Noda T. (2017). Autophagy in the context of the cellular membrane-trafficking system: the enigma of Atg9 vesicles. Biochem. Soc. Trans. 45, 1323–1331. [PubMed: 29150528]

Noda T, Kim J, Huang WP, Baba M, Tokunaga C, Ohsumi Y, and Klionsky DJ (2000). Apg9p/Cvt7p is an integral membrane protein required for transport vesicle formation in the Cvt and autophagy pathways. J. Cell Biol. 148, 465–480. [PubMed: 10662773]

Odorizzi G, Cowles CR, and Emr SD (1998). The AP-3 complex: a coat of many colours. Trends Cell Biol 8, 282–288. [PubMed: 9714600]

Ohashi Y, and Munro S. (2010). Membrane delivery to the yeast autophagosome from the Golgi-endosomal system. Mol. Biol. Cell 21, 3998–4008. [PubMed: 20861302]

Paix A, Folkmann A, and Seydoux G. (2017). Precision genome editing using CRISPR-Cas9 and linear repair templates in C. elegans. Methods 121–122, 86–93.

Pan PY, Sheehan P, Wang Q, Zhu X, Zhang Y, Choi I, Li X, Saenz J, Zhu J, Wang J, et al. (2020). Synj1 haploinsufficiency causes dopamine neuron vulnerability and alpha-synuclein accumulation in mice. Hum. Mol. Genet. 29, 2300–2312. [PubMed: 32356558]

Park SY, and Guo X. (2014). Adaptor protein complexes and intracellular transport. Biosci. Rep. 34, e00123.

Pirruccello M, and De Camilli P. (2012). Inositol 5-phosphatases: insights from the Lowe syndrome protein OCRL. Trends Biochem. Sci. 37, 134–143. [PubMed: 22381590]

Pokala N, Liu Q, Gordus A, and Bargmann CI (2014). Inducible and titratable silencing of Caenorhabditis elegans neurons in vivo with histamine-gated chloride channels. Proc. Natl. Acad. Sci. USA 111, 2770–2775. [PubMed: 24550306]

Popovic D, and Dikic I. (2014). TBC1D5 and the AP2 complex regulate ATG9 trafficking and initiation of autophagy. EMBO Rep. 15, 392–401. [PubMed: 24603492]

Puri C, Renna M, Bento CF, Moreau K, and Rubinsztein DC (2013). Diverse autophagosome membrane sources coalesce in recycling endosomes. Cell 154, 1285–1299. [PubMed: 24034251]

Puri C, Renna M, Bento CF, Moreau K, and Rubinsztein DC (2014). ATG16L1 meets ATG9 in recycling endosomes: additional roles for the plasma membrane and endocytosis in autophagosome biogenesis. Autophagy 10, 182–184. [PubMed: 24257061]

Quadri M, Fang M, Picillo M, Olgiati S, Breedveld GJ, Graafland J, Wu B, Xu F, Erro R, Amboni M, et al. (2013). Mutation in the SYNJ1 gene asso- ciated with autosomal recessive, early-onset Parkinsonism. Hum. Mutat. 34, 1208–1215. [PubMed: 23804577]

Raimondi A, Ferguson SM, Lou X, Armbruster M, Paradise S, Giovedi S, Messa M, Kono N, Takasaki J, Cappello V, et al. (2011). Overlapping role of dynamin isoforms in synaptic vesicle endocytosis. Neuron 70, 1100–1114. [PubMed: 21689597]

Reggiori F, Tucker KA, Stromhaug PE, and Klionsky DJ (2004). The Atg1-Atg13 complex regulates Atg9 and Atg23 retrieval transport from the pre-autophagosomal structure. Dev. Cell 6, 79–90. [PubMed: 14723849]

Richmond JE, Davis WS, and Jorgensen EM (1999). UNC-13 is required for synaptic vesicle fusion in C. elegans. Nat. Neurosci. 2, 959–964. [PubMed: 10526333]

Rostaing P, Weimer RM, Jorgensen EM, Triller A, and Bessereau JL (2004). Preservation of immunoreactivity and fine structure of adult C. elegans tissues using high-pressure freezing. J. Histochem. Cytochem. 52, 1–12. [PubMed: 14688212]

Rout MP, and Field MC (2017). The evolution of organellar coat complexes and organization of the eukaryotic cell. Annu. Rev. Biochem. 86, 637–657. [PubMed: 28471691]

Saheki Y, and De Camilli P. (2012). Synaptic vesicle endocytosis. Cold Spring Harb. Perspect. Biol. 4, a005645.

Sawa-Makarska J, Baumann V, Coudevylle N, von Bülow S, Nogellova V, Abert C, Schuschnig M, Graef M, Hummer G, and Martens S. (2020). Reconstitution of autophagosome nucleation defines Atg9 vesicles as seeds for membrane formation. Science 369.

Schindelin J, Arganda-Carreras I, Frise E, Kaynig V, Longair M, Pietzsch T, Preibisch S, Rueden C, Saalfeld S, Schmid B, et al. (2012). Fiji: an open-source platform for biological-image analysis. Nat. Methods 9, 676–682. [PubMed: 22743772]

Schneider CA, Rasband WS, and Eliceiri KW (2012). NIH Image to ImageJ: 25 years of image analysis. Nat. Methods 9, 671–675. [PubMed: 22930834]

Schreij AM, Fon EA, and Mcpherson PS (2016). Endocytic membrane trafficking and neurodegenerative disease. Cell. Mol. Life Sci. 73, 1529–1545. [PubMed: 26721251]

Schuske KR, Richmond JE, Matthies DS, Davis WS, Runz S, Rube DA, Van Der Bliek AM, and Jorgensen EM (2003). Endophilin is required for synaptic vesicle endocytosis by localizing synaptojanin. Neuron 40, 749–762. [PubMed: 14622579]

Sekito T, Kawamata T, Ichikawa R, Suzuki K, and Ohsumi Y. (2009). Atg17 recruits Atg9 to organize the pre-autophagosomal structure. Genes Cells 14, 525–538. [PubMed: 19371383]

Shehata M, Matsumura H, Okubo-Suzuki R, Ohkawa N, and Inokuchi K. (2012). Neuronal stimulation induces autophagy in hippocampal neurons that is involved in AMPA receptor degradation after chemical long-term depression. J. Neurosci. 32, 10413–10422. [PubMed: 22836274]

Son JH, Shim JH, Kim KH, Ha JY, and Han JY (2012). Neuronal autophagy and neurodegenerative diseases. Exp. Mol. Med. 44, 89–98. [PubMed: 22257884]

Soukup SF, Kuenen S, Vanhauwaert R, Manetsberger J, Hernández- Díaz S, Swerts J, Schoovaerts N, Vilain S, Gounko NV, Vints K, et al. (2016). A LRRK2-dependent EndophilinA phosphoswitch is critical for macro- autophagy at presynaptic terminals. Neuron 92, 829–844. [PubMed: 27720484]

Soykan T, Haucke V, and Kuijpers M. (2021). Mechanism of synaptic protein turnover and its regulation by neuronal activity. Curr. Opin. Neurobiol. 69, 76–83. [PubMed: 33744822]

Stavoe AKH, Hill SE, Hall DH, and Colón-Ramos DA (2016). KIF1A/ UNC-104 transports ATG-9 to regulate neurodevelopment and autophagy at synapses. Dev. Cell 38, 171–185. [PubMed: 27396362]

Stavoe AKH, and Holzbaur ELF (2019). Autophagy in neurons. Annu. Rev. Cell Dev. Biol. 35, 477–500. [PubMed: 31340124]

Stepp JD, Huang K, and Lemmon SK (1997). The yeast adaptor protein complex, AP-3, is essential for the efficient delivery of alkaline phosphatase by the alternate pathway to the vacuole. J. Cell Biol. 139, 1761–1774. [PubMed: 9412470]

Südhof TC (1995). The synaptic vesicle cycle: a cascade of protein-protein interactions. Nature 375, 645–653. [PubMed: 7791897]

Sumitomo A, and Tomoda T. (2021). Autophagy in neuronal physiology and disease. Curr. Opin. Pharmacol. 60, 133–140. [PubMed: 34416525]

Suzuki K, Kirisako T, Kamada Y, Mizushima N, Noda T, and Ohsumi Y. (2001). The pre-autophagosomal structure organized by concerted functions of APG genes is essential for autophagosome formation. EMBO J. 20, 5971–5981. [PubMed: 11689437]

Taoufiq Z, Ninov M, Villar-Briones A, Wang HY, Sasaki T, Roy MC, Beauchain F, Mori Y, Yoshida T, Takamori S, et al. (2020). Hidden prote- ome of synaptic vesicles in the mammalian brain. Proc. Natl. Acad. Sci. USA 117, 33586–33596.

Trinh J, and Farrer M. (2013). Advances in the genetics of Parkinson disease. Nat. Rev. Neurol. 9, 445–454. [PubMed: 23857047]

Tsukada M, and Ohsumi Y. (1993). Isolation and characterization of autophagy-defective mutants of Saccharomyces cerevisiae. FEBS Lett. 333, 169–174. [PubMed: 8224160]

Vanhauwaert R, Kuenen S, Masius R, Bademosi A, Manetsberger J, Schoovaerts N, Bounti L, Gontcharenko S, Swerts J, Vilain S, et al. (2017). The SAC1 domain in synaptojanin is required for autophagosome maturation at presynaptic terminals. EMBO J. 36, 1392–1411. [PubMed: 28331029]

Verstreken P, Koh TW, Schulze KL, Zhai RG, Hiesinger PR, Zhou Y, Mehta SQ, Cao Y, Roos J, and Bellen HJ (2003). Synaptojanin is re- cruited by endophilin to promote synaptic vesicle uncoating. Neuron 40, 733–748. [PubMed: 14622578]

Vidyadhara DJ, Lee JE, and Chandra SS (2019). Role of the endolysosomal system in Parkinson's disease. J. Neurochem. 150, 487–506. [PubMed: 31287913]

Vijayan V, and Verstreken P. (2017). Autophagy in the presynaptic compartment in health and disease. J. Cell Biol. 216, 1895–1906. [PubMed: 28515275]

Wang T, Martin S, Papadopulos A, Harper C, Mavlyutov T, Niranjan D, Glass N, Cooper-White J, Sibarita JB, Choquet D, et al. (2015). Control of autophagosome axonal retrograde flux by presynaptic activity unveiled using botulinum neurotoxin type-A. J. Neurochem. 35, 6179–6194.

Watanabe S, Trimbuch T, Camacho-Pérez M, Rost BR, Brokowski B, Söhl-Kielczynski B, Felies A, Davis MW, Rosenmund C, and Jorgensen EM (2014). Clathrin regenerates synaptic vesicles from endosomes. Nature 515, 228–233. [PubMed: 25296249]

Webber JL, and Tooze SA (2010). New insights into the function of Atg9. FEBS Lett. 584, 1319–1326. [PubMed: 20083107]

Webber JL, Young ARJ, and Tooze SA (2007). Atg9 trafficking in mammalian cells. Autophagy 3, 54–56. [PubMed: 17102588]

White JG, Southgate E, Thomson JN, and Brenner S. (1986). The structure of the nervous system of the nematode Caenorhabditis elegans. Philos. Trans. R. Soc. Lond. B Biol. Sci. 314, 1–340. [PubMed: 22462104]

Wu F, Watanabe Y, Guo XY, Qi X, Wang P, Zhao HY, Wang Z, Fujioka Y, Zhang H, Ren JQ, et al. (2015). Structural basis of the differential function of the two C. elegans Atg8 homologs, LGG-1 and LGG-2, in autophagy. Mol. Cell 60, 914–929. [PubMed: 26687600]

Xuan Z, Yang S, Hill SE, Clark B, Manning L, and Colon-Ramos DA (2021). 08.19.457026. The active zone protein Clarinet regulates ATG-9 trafficking at synapses and presynaptic autophagy. bioRxiv, bioRxiv:2021. 08.19.457026.

Yamamoto H, Kakuta S, Watanabe TM, Kitamura A, Sekito T, Kondo-Kakuta C, Ichikawa R, Kinjo M, and Ohsumi Y. (2012). Atg9 vesicles are an important membrane source during early steps of autophagosome formation. J. Cell Biol. 198, 219–233. [PubMed: 22826123]

Yorimitsu T, and Klionsky DJ (2005). Autophagy: molecular machinery for self-eating. Cell Death Differ 12 (Suppl 2), 1542–1552. [PubMed: 16247502]

Young ARJ, Chan EYW, Hu XW, Köchl R, Crawshaw SG, High S, Hailey DW, Lippincott-Schwartz J, and Tooze SA (2006). Starvation and ULK1-dependent cycling of mammalian Atg9 between the TGN and endosomes. J. Cell Sci. 119, 3888–3900. [PubMed: 16940348]

Zavodszky E, Seaman MN, Moreau K, Jimenez-Sanchez M, Breusegem SY, Harbour ME, and Rubinsztein DC (2014). Mutation in VPS35 associated with Parkinson's disease impairs WASH complex association and inhibits autophagy. Nat. Commun. 5, 3828. [PubMed: 24819384]

Zhang F, Wang LP, Brauner M, Liewald JF, Kay K, Watzke N, Wood PG, Bamberg E, Nagel G, Gottschalk A, and Deisseroth K. (2007). Multimodal fast optical interrogation of neural circuitry. Nature 446, 633–639. [PubMed: 17410168]

Zhou C, Ma K, Gao R, Mu C, Chen L, Liu Q, Luo Q, Feng D, Zhu Y, and Chen Q. (2017). Regulation of mATG9 trafficking by Src- and ULK1-mediated phosphorylation in basal and starvation-induced autophagy. Cell Res 27, 184–201. [PubMed: 27934868]

Zou L, Tian Y, and Zhang Z. (2021). Dysfunction of synaptic vesicle endocytosis in Parkinson's disease. Front. Integr. Neurosci. 15, 619160.

Highlights

- ATG-9 is localized in small vesicles in nerve terminals
- ATG-9 vesicles undergo activity-dependent exo-endocytosis at presynaptic sites
- Mutations in endocytic proteins disrupt ATG-9 localization at synapses
- ATG-9 mislocalization is associated with defects in activity-induced synaptic autophagy

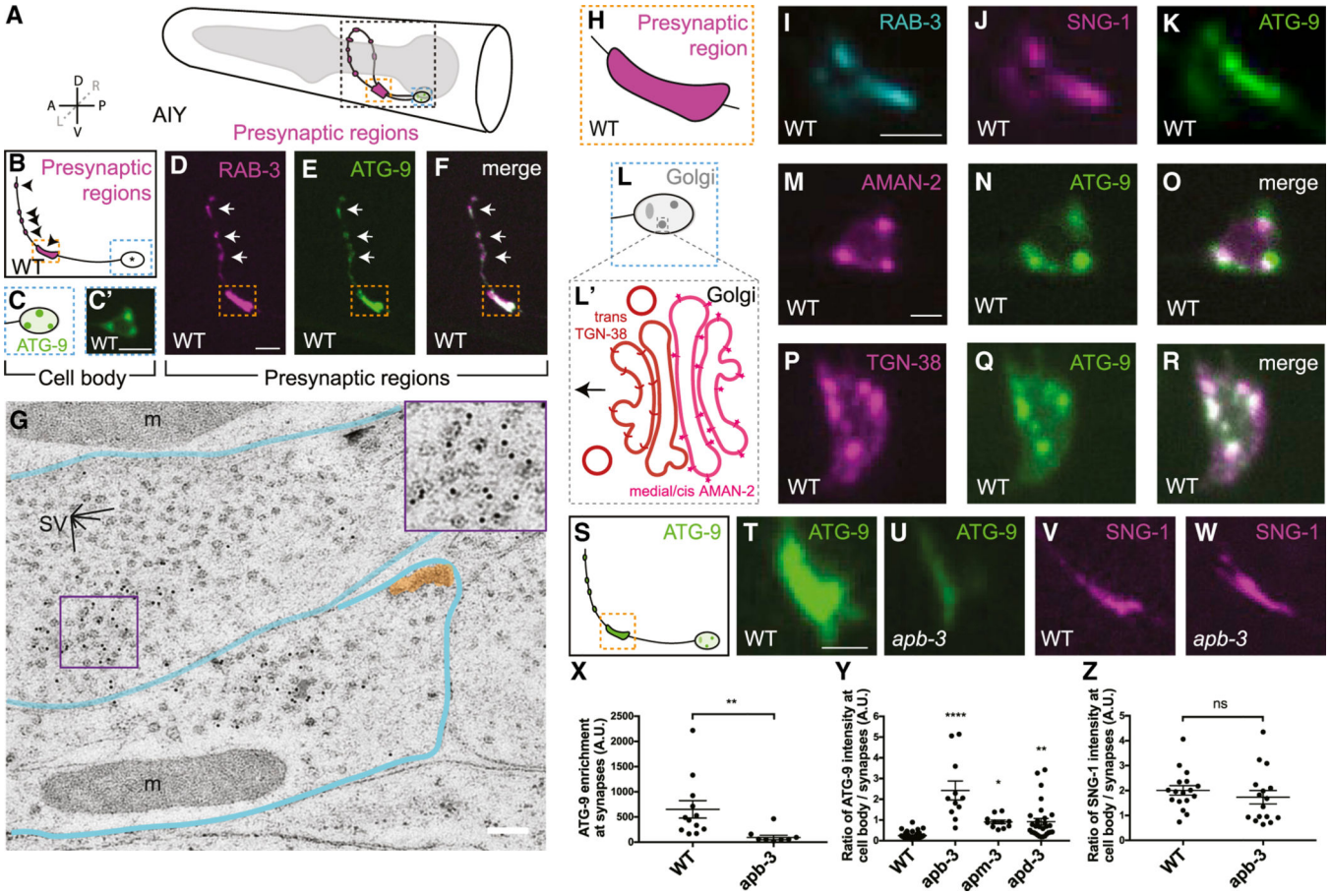

Figure 1. In *C. elegans* ATG-9 is transported to synapses in vesicles generated in the *trans*-Golgi network (TGN) via AP-3-dependent budding

(A) Schematic of the head of *C. elegans*, including pharynx (gray region) and the two bilaterally symmetric AIY interneurons (in black dashed box) with presynaptic regions (magenta). The synaptic-rich region is highlighted with an orange dashed square and cell bodies with a blue dashed square. In axis, A, anterior; P, posterior; L, left; R, right; D, dorsal; V, ventral.

(B) Schematic of a single AIY interneuron with cell body (in blue dashed square) and presynaptic regions (magenta and black arrowheads, and synaptic-rich region highlighted with an orange dashed square). See Figures S1A–S1F for electron microscopy reconstructions of presynaptic regions in AIY.

(C) Schematic of a cell body in the AIY interneurons, with ATG-9 localization represented in green. (C′) Representative confocal micrograph of ATG-9::GFP localization at the cell body of AIY in a wild-type animal (as in C, and blue dashed box in B).

(D–F) Representative confocal micrographs of RAB-3::mCherry (magenta) (D), ATG-9::GFP (E), and merged channels (F) in the synaptic regions of a representative wild-type AIY interneuron. The arrows and the dashed box highlight the presynaptic specializations.

(G) Immunogold electron microscopy of transgenic animals with panneuronal expression of ATG-9::GFP, with antibodies directed against GFP (see Figures S1G– S1J). Blue line,

outline of neurons. (presynaptic) dense projections, shaded in orange. “m,” mitochondria. “SV,” examples of synaptic vesicles (pointed with lines). Purple square, representative region and enlarged image of ATG-9 localizing to synaptic vesicles.

(H) Schematic of synaptic-rich region in the AIY interneurons (corresponding to orange dashed box region in B).

(I–K) Representative confocal micrographs of RAB-3::mCherry (cyan) (I), SNG-1::BFP (magenta) (J), and ATG-9::GFP (K) at synaptic-rich region (corresponding to H, also orange dashed box in B) in wild-type. See Figures S1K–S1M for merged channels.

(L) Schematic of the AIY interneuron cell body with Golgi labeled (as gray puncta), (L′) schematic of the Golgi apparatus with medial/*cis*-Golgi-specific protein AMAN-2 (magenta), and *trans*-Golgi-specific protein TGN-38 (crimson).

(M–O) Confocal micrographs of AMAN-2::GFP (magenta) (M), ATG-9::mCherry (green) (N), and merged channels (O) at the cell body of AIY.

(P–R) Confocal micrographs of TGN-38::mCherry (magenta) (P), ATG-9::GFP (Q), and merged channels (R) at the cell body of AIY. See Figures S2A–S2H for colocalization analyses with other organelles markers.

(S) Schematic of an AIY interneuron with ATG-9 (green). Presynaptic-rich region (Zone 2) is highlighted by orange rectangle.

(T and U) Confocal micrographs of ATG-9::GFP at Zone 2 in wild type (T) and *apb-3(ok429)* mutants (U).

(V and W) Confocal micrographs of SNG-1::GFP (magenta) at Zone 2 in wild type (V) and *apb-3(ok429)* mutants (W).

(X) Quantification of ATG-9::GFP enrichment at Zone 2 of AIY neurons in wild-type and *apb-3(ok429)* mutant animals. Error bars correspond to standard error of the mean (SEM). **p < 0.01 by Welch’s t test between wild-type and mutant animals.

(Y) Quantification of the ratio of ATG-9 intensity at cell body/synapses of AIY neurons in wild-type, *apb-3(ok429)*, *apm-3(gk771233)*, and *apd-3(gk805642)* mutant animals. Error bars correspond to SEM. *p < 0.05, **p < 0.01, and ****p < 0.0001 (between wild-type and the mutants) by ordinary one-way ANOVA with Dunnett’s multiple comparisons test between wild-type and the mutant groups.

(Z) Quantification of ratio of SNG-1 intensity at cell body/synapses of AIY neurons in wild-type and *apb-3(ok429)* mutant animals. “ns”: not significant (between wild-type and the mutants) by Welch’s t test between wild-type and mutant animals.

Scale bars: 5 μm in (C′) and 5μm in (D) for (D)–(F); 200 nm in (G) and 2 μm in (I) for (I)–(K); 2 μm in (M) for (M)–(R); 2 μm in (T) for (T)–(W).

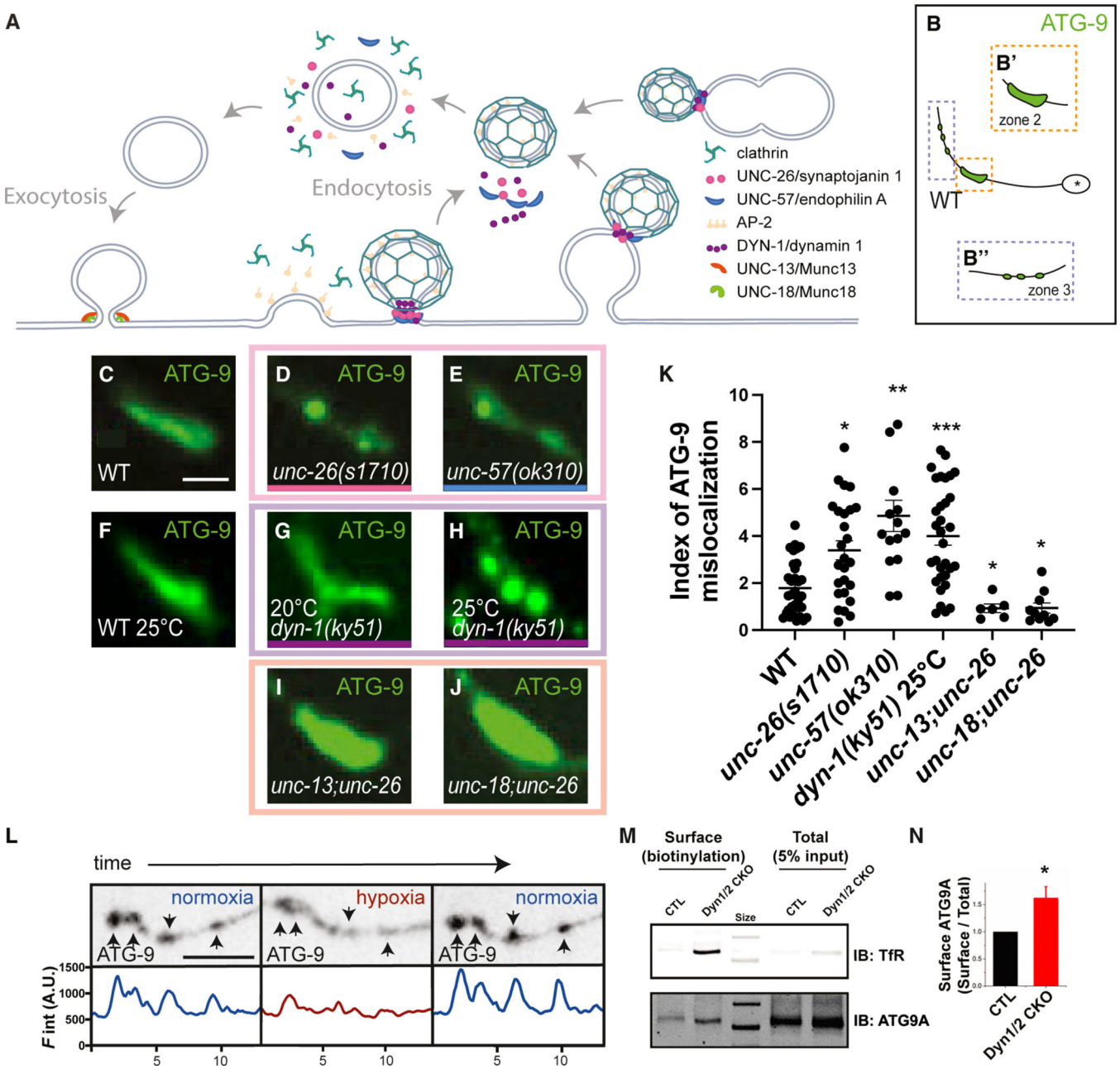

Figure 2. ATG-9 undergoes exo-endocytosis at presynaptic sites

(A) Schematic of the proteins required for the synaptic vesicle cycle examined in this study, with vertebrate and *C. elegans* protein names.

(B) Schematic of ATG-9 localization in AIY neurons (B), enlargement of the synaptic-rich region termed Zone 2 (B′ and orange dashed box), and distal part of the neurite with synaptic clusters, termed Zone 3 (B″ and purple dashed box).

(C–E) Confocal micrographs of ATG-9::GFP at AIY Zone 2 in wild type (C), *unc-26(s1710)* (D), and *unc-57(ok310)* (E) mutants.

(F–H) As (C–E) but with wild type at 25°C (F) and a temperature-sensitive *dyn-1(ky51)* mutants at the permissive temperature 20°C (G), at the restrictive temperature 25°C (H).

(I and J) *unc-13(s69);unc-26(e205)* (I) and *unc-18(e81);unc-26(s1710)* (J) double mutants. See Figures S3H and S3I for confocal micrographs of ATG-9::GFP in *unc-13(s69)* and *unc-18(e81)* single mutants.

(K) Quantification of the index of ATG-9 mislocalization (see STAR Methods) in wild type, *unc-26(s1710)*, *unc-57(ok310)*, and *dyn-1(ky51)* mutants at 25°C, *unc-13(s69);unc-26(e205)* and *unc-18(e81);unc-26(s1710)* double mutants. Except for *dyn-1(ky51)* mutants, all the other genotypes were examined at room temperature. Error bars show SEM. *$p < 0.05$, **$p < 0.01$, and ***$p < 0.001$ (between wild-type and the mutants) by ordinary one-way ANOVA with Dunnett's multiple comparisons test between wild-type and the mutant groups. See Figure S3A for quantification of penetrance of ATG-9 mislocalization.

(L) Confocal micrographs of ATG-9::GFP (black) at AIY Zone 3 (see B″) in *pfk-1.1*(*gk922689*) mutants under normoxia (left panels), after 10 min of transient hypoxia (middle panels), and another iteration of 10 min of normoxia (right panels). Corresponding fluorescence intensity is shown below the line scan image (see also Figure S3L).

(M and N) Surface levels of ATG9A and transferrin receptor (TfR) in control and dynamin 1 and 2 conditional double-knockout (Dyn1/2 CKO) fibroblasts. (M) Immunoblots (IB) for transferrin receptor (TfR) and ATG9A of total cell extracts and of material recovered by streptavidin affinity purification following surface biotinylation. See Figures S5A–S5C for quantification of TfR and immunoblots of dynamin 1 and 2. (N) Quantification of surface/total levels of ATG9A in Dyn1/2 CKO fibroblasts relative to the control cells (CTL). Error bars show SEM. *$p < 0.05$ by Student's t test.

Scale bars: 2 μm in (C) for (C)–(J); 5 μm in (L).

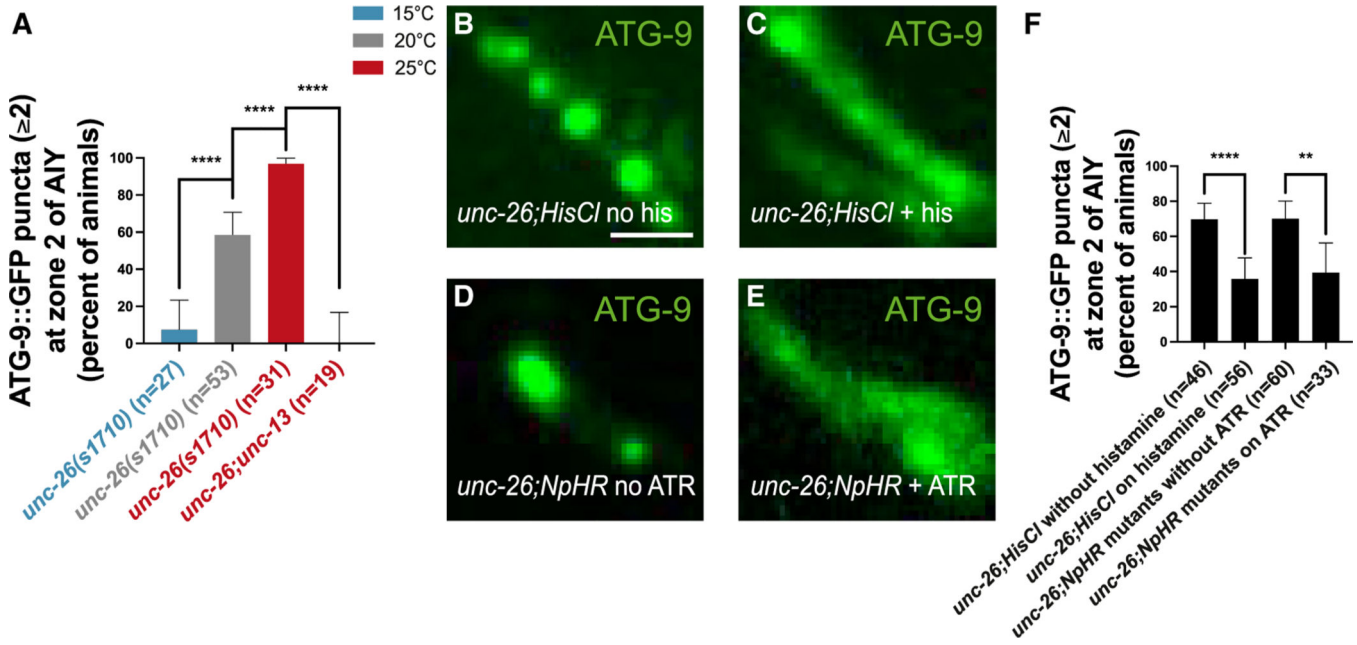

Figure 3. ATG-9 mislocalization phenotypes can be predictably altered by manipulating the AIY activity state

(A) Quantification of the percentage of animals displaying two (or more) ATG-9 subsynaptic foci at AIY Zone 2 in *unc-26(s1710)* mutants raised at 15°C (blue), 20°C (gray), and 25°C (red). Higher temperatures result in an increased activity state in AIY (Hawk et al., 2018) (Figures S4A–S4C), and autophagy (Hill et al., 2019). *unc-13(s69);unc-26(e205)* double mutants were also raised at 25°C and quantified (red). Error bars show 95% confidence intervals. ****p < 0.0001 by two-tailed Fisher's exact test.

(B and C) Confocal micrographs of ATG-9::GFP at AIY Zone 2 in *unc-26(s1710)* mutants expressing the heterologous *Drosophila* inhibitory chloride channel (HisCl) without histamine (B) or exposed to histamine (C).

(D and E) Confocal micrographs of ATG-9::GFP at AIY Zone 2 in *unc-26(s1710)* mutants expressing the inhibitory light-driven chloride pump (NpHR) in AIY, without cofactor ATR (D) or with cofactor ATR (E) and under the light (see STAR Methods).

(F) Quantification of the percentage of animals displaying two (or more) ATG-9 subsynaptic foci at AIY Zone 2 in *unc-26(s1710)* mutants expressing HisCl and mutants expressing NpHR. Mutants expressing HisCl were raised at 15°C and incubated at 25°C for one day with or without the histamine. Note that inhibition of AIY activity (expressing the HisCl in the presence of histamine under light) results in a partial suppression of ATG-9 synaptic foci. The difference between the control condition for this experiment and *unc-26(s1710)* mutants raised at 25°C is accounted for in the difference of the rearing of these animals (see STAR Methods). *unc-26(s1710)* mutants expressing NpHR were raised at 20°C. Error bars show 95% confidence intervals. **p < 0.01 and ****p < 0.0001 by two-tailed Fisher's exact test.

Scale bars: 2 μm in (B) for (B)–(E).

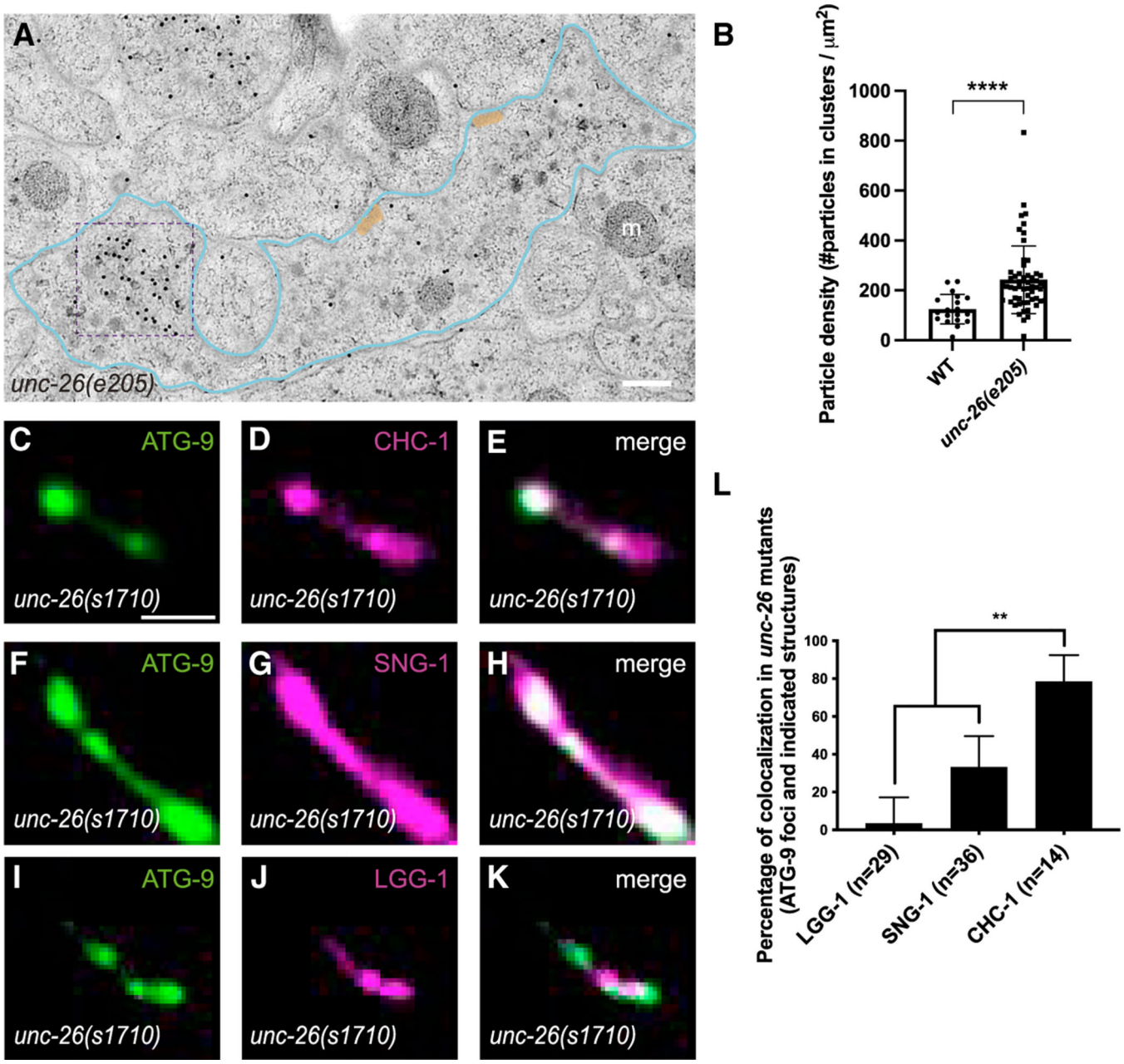

Figure 4. In *unc-26/synaptojanin 1* mutants, ATG-9 accumulates at presynaptic, clathrin-rich sites

(A) Immunogold electron microscopy of transgenic animals with panneuronal expression of ATG-9::GFP in AIY in *unc-26(e205)* mutants, with antibodies directed against GFP. Note that the majority of immunogold particles accumulate in the clustered vesicles. Blue line, outline of neurons. Dense projections, shaded in orange. “m,” mitochondria. Purple square with dashed lines emphasizes and area with immunogold particles at the clustered vesicles. (B) Density of immunogold particles on the clustered vesicles in wild type and *unc-26(e205)* mutants. Each dot in the scatter plot represents a section. ****$p < 0.0001$ by Welch’s t test. See Figure S5D for quantification of the number of immunogold particles on vesicles.

(C–E) Confocal micrographs of ATG-9::GFP (C), BFP::clathrin heavy chain (CHC-1) (magenta) (D), and merged channels (E) at AIY Zone 2 in *unc-26(s1710)* mutants.
(F–H) Confocal micrographs of ATG-9::GFP (F), SNG- 1::BFP (magenta) (G), and merged channels (H) in *unc-26(s1710)* mutants.
(I–K) Confocal micrographs of ATG-9::mCherry (green) (I), GFP::LGG-1 (magenta) (J), and merged channels (K) in *unc-26(s1710)* mutants.
(L) Percentage of ATG-9 foci that colocalize with LGG-1/Atg8/GABARAP, with SNG-1/synaptogyrin or with CHC-1/Clathrin heavy chain puncta in *unc-26(s1710)* mutants. The numbers of foci examined in each condition are indicated by the "n." Error bars show 95% confidence intervals. **$p < 0.01$ by two-tailed Fisher's exact test.
Scale bars: 200 nm in (A); 2 μm in (C) for (C)–(K).

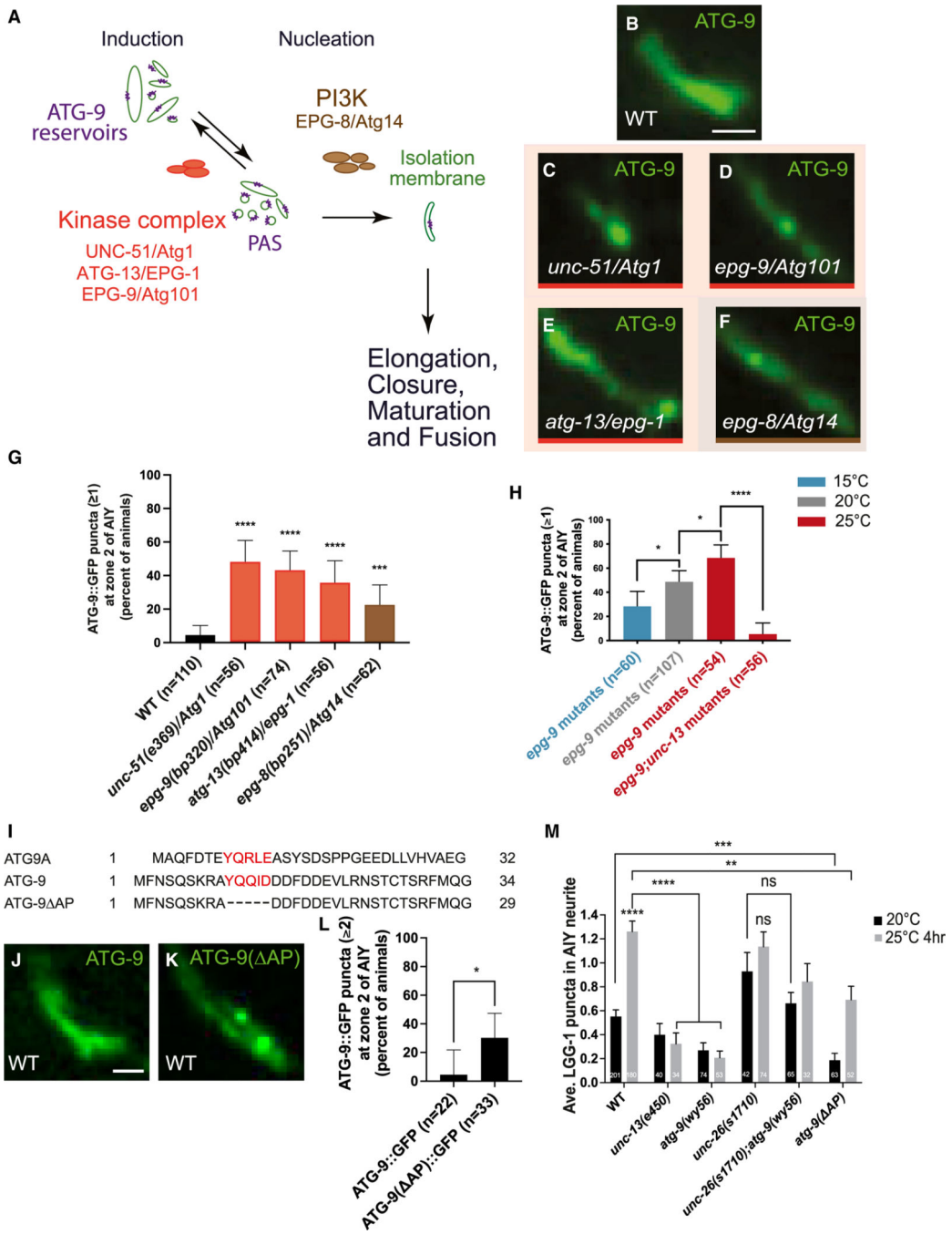

Figure 5. ATG-9 trafficking is affected in autophagy mutants and affects synaptic autophagy

(A) Schematic of the autophagosome biogenesis pathway. ATG-9 cycles between ATG-9 reservoirs and pre-autophagosomal structures (PAS) during autophagosome biogenesis (Reggiori et al., 2004; Yamamoto et al., 2012; Suzuki et al., 2001).

(B–F) Confocal micrographs of ATG-9::GFP at AIY Zone 2 in wild type (B), *unc-51(e369)/Atg1* (C), *epg-9(bp320)/Atg101* (D), *atg-13(bp414)/epg-1* (E), and *epg-8(bp251)/Atg14* (F) mutants.

(G) Quantification of percentage of animals displaying one (or more) ATG-9 subsynaptic foci at AIY Zone 2 in wild type and indicated autophagy mutants. Error bars show 95% confidence intervals. ***p < 0.001 and ****p < 0.0001 (between wild-type and the mutants) by two-tailed Fisher's exact test.

(H) Quantification of the percentage of animals with one (or more) ATG-9 subsynaptic foci at AIY Zone 2 in *epg-9(bp320)/Atg101* mutants raised at 15°C (blue), 20°C (gray), and 25°C (red). *Unc-13(s69);epg-9(bp320)* double mutants were also raised at 25°C and quantified (red). *p < 0.01 and ****p < 0.0001 by two-tailed Fisher's exact test.

(I) Sequence alignment between the N-terminal cytosolic tail of the human ATG9A (N terminus on the left), the *C. elegans* ATG-9, and the *C. elegans* ATG-9(ΔAP). Conserved binding motifs between ATG9A/ATG-9 and AP-2 are highlighted in red (Imai et al., 2016).

(J and K) Confocal micrographs of AIY synaptic Zone 2 in the wild-type animals expressing ATG-9::GFP (J) or ATG-9(ΔAP)::GFP (K), which lacks a canonical motif predicted to bind sorting complexes, such as AP-2 (Imai et al., 2016).

(L) Quantification of the percentage of wild-type animals with two (or more) ATG-9::GFP or ATG-9(ΔAP)::GFP subsynaptic foci at AIY Zone 2. Error bars show 95% confidence intervals. *p < 0.05 by two-tailed Fisher's exact test.

(M) Quantification of the number of LGG-1 puncta in the AIY neurites at 20°C and at 25°C for 4 h in wild type, *unc-13(e450)*, *atg-9(wy56)*, *unc-26(s1710)*, *unc-26(s1710);atg-9(wy56)*, and *atg-9(ΔAP)* mutants. In *unc-26* mutants, LGG-1 puncta are observed in the neurite but are likely corresponding to defective autophagosomes as they are not suppressed in *unc-26;atg-9* double mutants nor are they induced by increased activity state. *atg-9(ΔAP)* mutants display a reduction of LGG-1 puncta, although LGG-1 increases upon conditions that increase the neuronal activity state. "ns" (not significant) and ****p < 0.0001 (between 20°C and 25°C in each genotype) by Welch's t test. "ns" (not significant), **p < 0.01, ***p < 0.001, and ****p < 0.0001 (between genotypes) by ordinary one-way ANOVA with Dunnett's multiple comparisons test between wild-type and the mutant groups. See Figures S7D–S7G for representative images.

Scale bars: 2 μm in (B) for (B)–(F); 2 μm in (J) for (J) and (K).

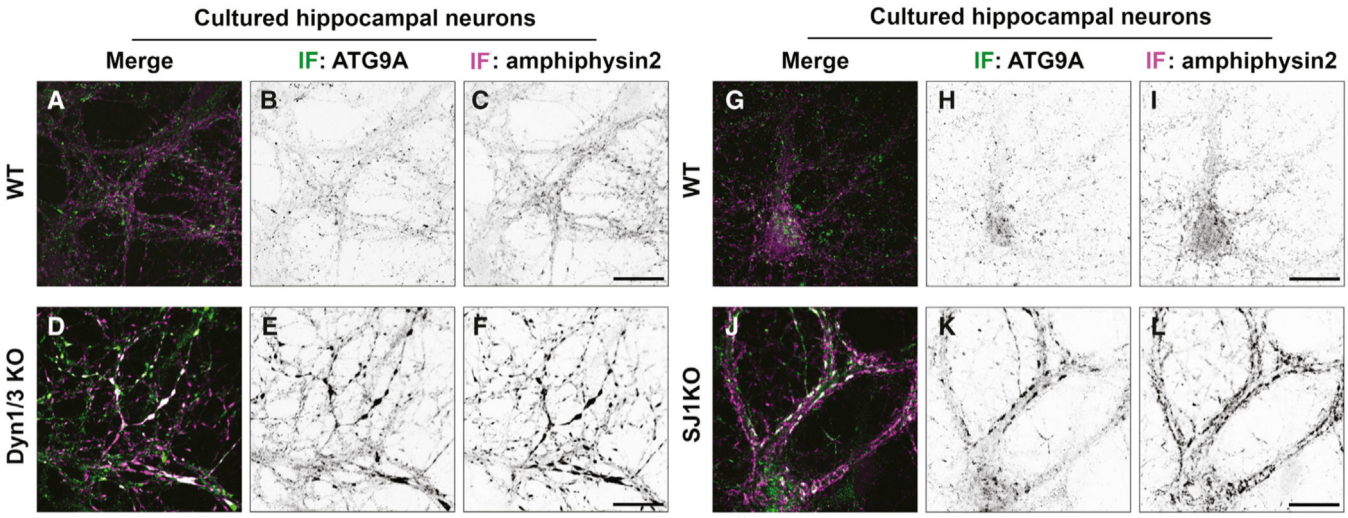

Figure 6. Abnormal accumulation of ATG9A in nerve terminals of mammalian neurons with mutations in endocytic proteins

(A–F) Representative images showing immunoreactivity for ATG9A (B and E), amphiphysin 2 (C and F), and merged channels (A and D) in DIV17 hippocampal neuronal cultures from wild-type (WT) (A–C) and dynamin 1/3 double KO (Dyn1/3 KO) (D–F) newborn mice.

(G–L) Representative images showing immunoreactivity for ATG9A (H and K) and amphiphysin 2 (I and L) in DIV23 hippocampal neuronal cultures from wild-type (WT) (G–I) and synaptojanin1 KO (SJ1 KO) (J–L) newborn mice. See Figure S8A for quantification on the ATG9A phenotype.

Scale bars: 20 μm in (C), (F), (I), and (L) for (A)–(L).

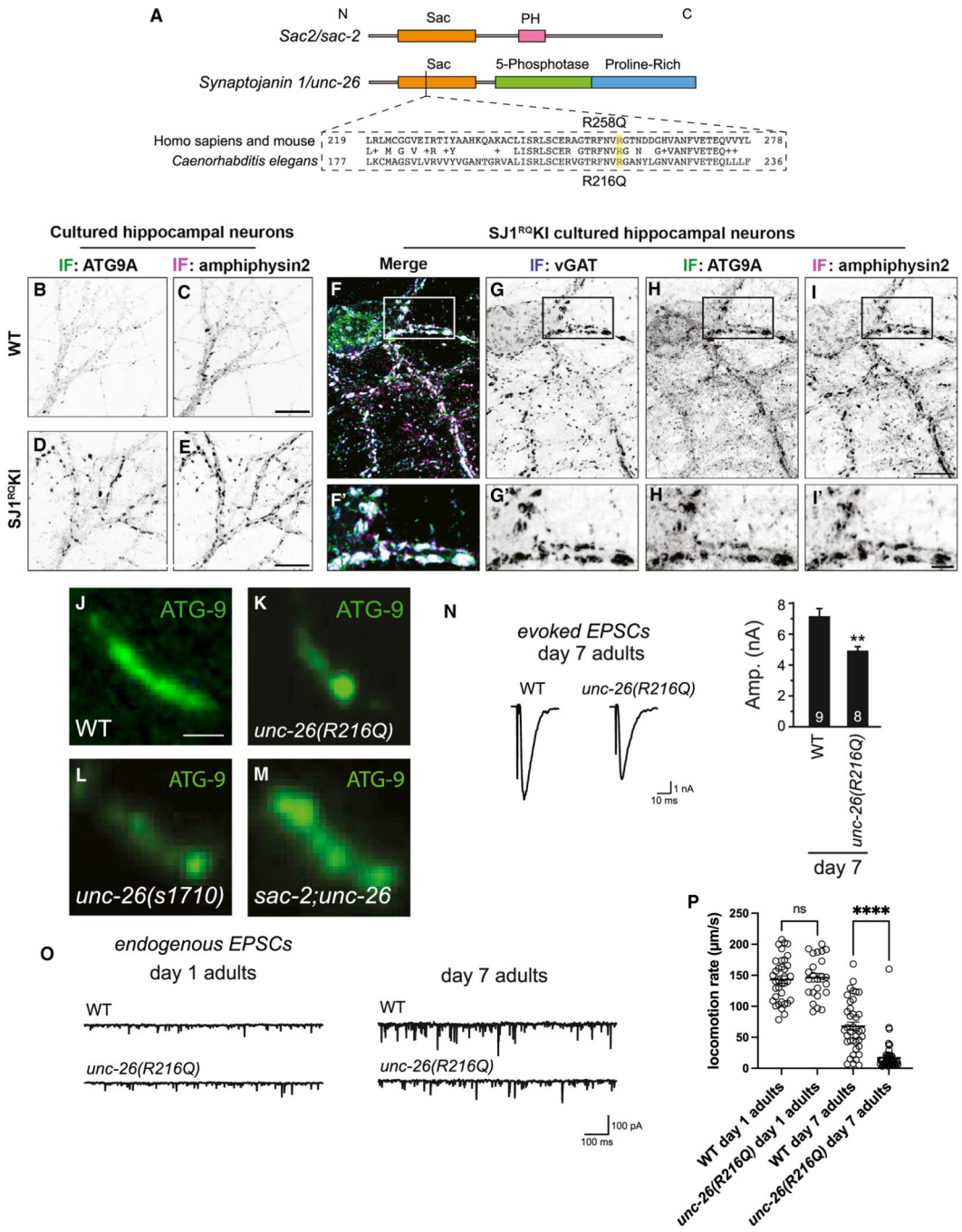

Figure 7. A mutation in *unc-26/synaptojanin 1* associated with early-onset Parkinsonism (EOP) leads to abnormal focal accumulation of ATG- and age-dependent electrophysiological and behavioral phenotypes

(A) Domain structures of *Sac2/sac-2* and *synaptojanin 1/unc-26*. The mutated residue associated with EOP is conserved (highlighted in yellow) (Quadri et al., 2013; Krebs et al., 2013).

(B–E) Representative images showing immunoreactivity for ATG9A (B and D), amphiphysin 2 (C and E) in DIV23 hippocampal neuronal cultures from newborn wild-type

(WT) (B and C) and mutant mice harboring an EOP associated mutation in the synaptojanin 1 ($SJ1^{RQ}KI$) gene (D and E).

(F–I) Representative images showing immunoreactivity for vesicular GABA transporter (vGAT) (G), ATG9A (H), amphiphysin 2 (I), and merged channels (F) in DIV19 hippocampal neuronal cultures from $SJ1^{RQ}KI$ newborn mice. (F′–I′) Enlarged images of squared regions in (F–I). See Figure S8A for quantification on the ATG9A phenotype.

(J–M) Representative confocal micrographs of ATG-9::GFP at AIY Zone 2 in wild type (J), *unc-26(R216Q)* (K) mutants, *unc-26(s1710)* (L), and *sac-2(gk346019);unc-26(s1710)* (M) mutants. See Figures S8B and S8C for quantification on the ATG-9 phenotype.

(N) Representative traces and summary data for evoked EPSC amplitude in wild-type and *unc-26(R216Q)* mutants of 7-day-old adults. Error bars show SEM. **p < 0.01 by Student's t test between wild-type and mutant animals. See Figures S8K and S8L for quantification of 1-day-old adults.

(O) Representative traces for endogenous EPSC rates in wild type and *unc-26(R216Q)* mutants of 1-day-old adults and 7-day-old adults. See Figures S8M and S8N for quantification of the endogenous EPSC rates.

(P) Quantification of locomotion rate in wild type and *unc-26(R216Q)* mutants of 1-day-old adults and 7-day-old adults. Error bars show SEM. "ns" (not significant) and ****p < 0.0001 by Student's t test between wild-type and mutant animals.

Scale bars: 20 μm in (B) for (B and C); 20 μm in (D) for (D and E); 20 μm in (F) for (F and I); 5 μm in (F′) for (F′ and I′); 2 μm in (J) for (J–M).

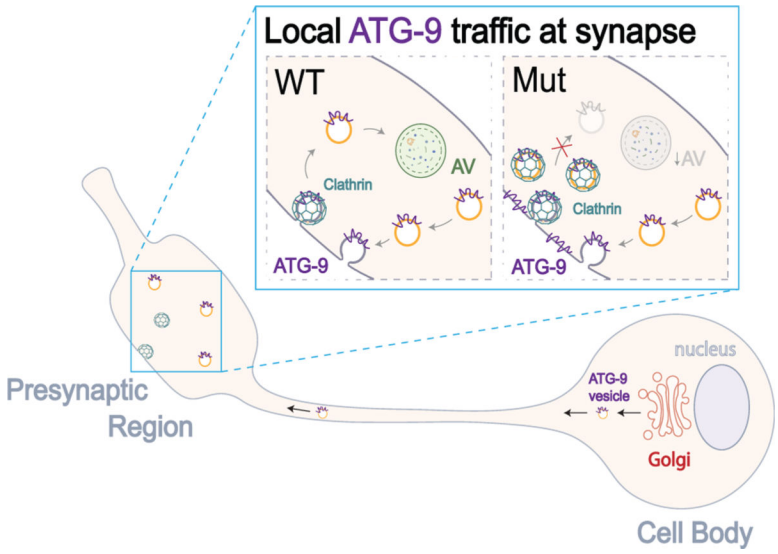

Figure 8. A model for ATG-9 neuronal trafficking, from the cell body to the synapse

Schematic model of ATG-9 trafficking in *C. elegans* neurons. ATG-9 vesicles originate from the *trans*-Golgi network via AP-3-dependent budding (*C. elegans* lacks AP-4 adaptors). Once ATG-9 vesicles reach the presynaptic region via UNC-104/KIF1A transport (Stavoe et al., 2016) they undergo exo-endocytosis. In mutants that disrupt endocytosis, or in autophagy mutants, ATG-9 accumulates into clathrin-enriched synaptic foci, and activity-induced presynaptic autophagy is compromised. Similar mechanisms operate at mammalian nerve terminals.

KEY RESOURCES TABLE

REAGENT or RESOURCE	SOURCE	IDENTIFIER
Chemicals		
Cold Water Fish Skin Gelatin	Aurion	SKU#900.033
Anhydrous Acetone (glass distilled)	Electron Microscopy Sciences (EMS)	Cat#10015; CAS: 67–64-1
Bovine Serum Albumin	EMS	Cat#25554
EMBed-812 Embedding Kit	EMS	Cat#14120
Glutaraldehyde (10% in acetone)	EMS	Cat#16530
Lead Nitrate	EMS	Cat#17900; CAS: 10099–74-8
Lowicryl HM20	EMS	Cat#14340
Osmium Tetroxide	EMS	Cat#19100; CAS: 20816–12-0
Sodium Citrate	EMS	Cat#21140; CAS: 6132–04-3
Tannic Acid	EMS	Cat#21700; CAS: 1401–55-4
Uranyl acetate	EMS	Cat#22400; CAS: 541–09-3
Ammonium chloride	Millipore	Cat#1011450500; CAS: 12125–02-9
1-Hexadecene	Sigma-Aldrich	SKU#H2131; CAS: 629–73-2
4-Hydroxytamoxifen	Sigma-Aldrich	SKU#H6278; CAS: 68392–35-8
Glycine powder	Sigma-Aldrich	SKU#G7126; CAS: 56–40-6
Levamisole Hydrochloride	Sigma-Aldrich	SKU#PHR1798; CAS: 16595–80-5
EZ-Link™ Sulfo-NHS-LC-Biotin	Thermo Scientific	Cat#21335
NeutrAvidin Agarose Resin	Thermo Scientific	Cat#29200
PierceTM BCA Protein Assay Kit	Thermo Scientific	Cat#23225
Protein A Gold 10 nm	University Medical Center Utrecht	Order: PAG 10 nm/S

REAGENT or RESOURCE	SOURCE	IDENTIFIER
Chemicals		
Toluidine Blue	Ward's Science	Item#470302–956; CAS: 92–31-9
Experimental Models: Organisms/Strains		
C. elegans: olaIs34 [DACR808 (pttx-3::atg-9::gfp) (10 ng/μl) + DACR18 (pttx-3:mCh:rab-3) (30 ng/μl)] III	This paper	DCR4755
C. elegans: olaex2264 [DACR1821 (punc-14::atg-9::GFP)(5ng/μl)]	(Stavoe et al., 2016)	DCR4535
C. elegans: olaex2264	This paper	DCR4535
C. elegans: unc-26(e205);olaex2264	This paper	DCR5952
C. elegans: unc-101(m1) I	Caenorhabditis Genetics Center	DR1
C. elegans: unc-101(m1);olaIs34	This paper	DCR8064
C. elegans: dpy-23(e840) X	Caenorhabditis Genetics Center	CB840
C. elegans: dpy-23(e840);olaIs34	This paper	DCR8633
C. elegans: apb-3(ok429) I	Caenorhabditis Genetics Center	RB662
C. elegans: apb-3(ok429);olaIs34	This paper	DGR7823
C. elegans: olaex4060 [DAGR922 (pttx-3::atg-9::mCh) (20ng/μl) + DAGR2716 (pttx-3::sng-1::gfp) (15ng/μl)]	This paper	DGR6797
C. elegans: apb-3(ok429);olaex4060	This paper	DGR8584
C. elegans: apm-3(gk771233) X	Caenorhabditis Genetics Center	VG40707
C. elegans: apm-3(gk771233);olaIs34	This paper	DGR8058
C. elegans: apd-3(gk805642) II	Caenorhabditis Genetics Center	VG40775
C. elegans: apd-3(gk805642);olaIs34	This paper	DGR8135
C. elegans: olaEx4710 [DAGR941 (pttx-3::aman-2::gfp) (0.5ng/μl) + DAGR922 (pttx-3::atg-9::mCh) (20ng/μl)]	This paper	DGR8018
C. elegans: olaEx4966 [DAGR808 (pttx-3::atg-9::gfp) (10ng/μl) + DAGR3393 (pttx-3::tgn-38::mCh) (20ng/μl)]	This paper	DGR8582
C. elegans: olaEx4805 [DGR930 (pttx-3::sp12::GFP) (5ng/μl) + DAGR922 (pttx-3::atg-9::mCh) (20ng/μl)]	This paper	DGR7899
C. elegans: olaEx5178 [DAGR1617 (pttx-3::tomm-20::gfp) (30 ng/μl) + DAGR18 (pttx-3::atg-9::mCh) (30 ng/μl)]	This paper	DGR8567
C. elegans: unc-26(s1710) IV	Caenorhabditis Genetics Center	EG3027
C. elegans: unc-26(e205) IV	Caenorhabditis Genetics Center	GB205
C. elegans: unc-26(e205);olaIs34	This paper	DGR5578
C. elegans: unc-26(s1710);olaIs34	This paper	DGR6121
C. elegans: unc-26(pek228[unc-26_R216Q]) IV	This paper	BJH728

REAGENT or RESOURCE	SOURCE	IDENTIFIER
Chemicals		
C. elegans: unc-57(ok310) I	Kang Shen Laboratory (Stanford University, California) (Li et al., 2016; Schuske et al., 2003)	EG2710
C. elegans: unc-57(ok310);olaIs34	This paper	DGR5599
C. elegans: unc-11(e47) I	Caenorhabditis Genetics Center	GB47
C. elegans: unc-11(e47);olaIs34	This paper	DGR5893
C. elegans: dyn-1(ky51) X	Caenorhabditis Genetics Center	GX51
C. elegans: dyn-1(ky51);olaIs34	This paper	DGR5953
C. elegans: unc-18(e81) X	Caenorhabditis Genetics Center	GB81
C. elegans: unc-18(e81);olaIs34	This paper	DGR8033
C. elegans: unc-18(e81);unc-26(s 1710);olaIs34	This paper	DGR8387
C. elegans: unc-13(s69) I	Erik Jorgensen Laboratory (University of Utah, Salt Lake City, Utah) (Richmond etal., 1999)	BG168
C. elegans: unc-13(s69);olaIs34	This paper	DGR5598
C. elegans: unc-13(s69);unc-26(e205);olaIs34	This paper	DGR6406
C. elegans: unc-26(s 1710);olaex3465;olaIs34	This paper	DGR7497
C. elegans: olaIs17 [pmod-1::GCaMP6s;pttx-3::mCherry;punc-122:dsRed]	(Hawk etal., 2018)	DGR3056
C. elegans: *xuIs230* (pttx-3s::NpHR::yfp;pttx-3s::DsRed;punc-*122::yfp);unc-26(s1710);olaIs34*	This paper	DCR8661
C. elegans: olaEx4099 [DACR2739 (pttx-3::sng-1::bfp) (30ng/|µl)];olaIs34	This paper	DCR6894
C. elegans: *olaEx4099* [DACR2739 (pttx-3::sng-1::bfp) (30ng/µl)];unc-*26(s1710);olaIs34*	This paper	DCR6877
C. elegans: *olaEx4020* [DACR2739 (pttx-3::sng-1::bfp) (30ng/µl) + DACR808 (pttx-3::atg-9::gfp) (10ng/µl)]	This paper	DCR6710
C. elegans: unc-26(s1710);olaex4020	This paper	DCR6838
C. elegans: olaEx3462 [DACR4860 (pttx-3::unc-26) *(5ng/µl)];unc-26(e205);olaIs34*	This paper	DCR5950
C. elegans: unc-26(s1710);olaEx1360 [DACR922 (pttx-3::mCh::atg-9) (30 ng/µl)];olaIs44 [DACR1321 (pttx-3::gfp::lgg-1) (15ng/µl)]	This paper	DCR7339
C. elegans: unc-26(s1710);olaex4290 [DACR2877 (pttx-3::bfp::chc-1) (5ng/µl)];*olaIs34*	This paper	DCR7332
C. elegans: epg-9(bp320);olaex4290;olaIs34	This paper	DCR8924
C. elegans: pfk-1.1(gk922689) X	Caenorhabditis Genetics Center	VC41001
C. elegans: pfk-1.1(gk922689);olaIs34	This paper	DCR6129
C. elegans: pfk-1.1(gk922689);unc-13(s69);olaIs34	This paper	DCR8873

REAGENT or RESOURCE	SOURCE	IDENTIFIER
Chemicals		
C. elegans: unc-51(e369) V	Caenorhabditis Genetics Center	CB369
C. elegans: unc-51(e69);olaIs34	This paper	DCR7527
C. elegans: epg-9(bp320) IV	Caenorhabditis Genetics Center	HZ1692
C. elegans: epg-9(bp320);olaIs34	This paper	DCR7047
C. elegans: epg-9(bp320);unc-13(s69);olaIs34	This paper	DCR8869
C. elegans: epg-8(bp251) I	Caenorhabditis Genetics Center	HZ1691
C. elegans: epg-8(bp251);olaIs34	This paper	DCR7048
C. elegans: atg-13(bp414) III	Caenorhabditis Genetics Center	HZ1688
C. elegans: olaIs33 [DACR808 (pttx-3::atg-9::gfp) (10 ng/μl) + DACR18 (pttx-3::mCh::rab-3) (30 ng/μl)]	This paper	DCR4654
C. elegans: atg-13(bp414);olaIs33	This paper	DCR7479
C. elegans: olaEx4718 [DACR3209 (pttx-3::atg-9(ΔAP)::gfp) (10ng/μl)]	This paper	DCR7770
C. elegans: olaEx4719 [DACR3209 (pttx-3::atg-9(ΔAP)::gfp) (10ng/μl)]	This paper	DCR7771
C. elegans: olaIs35 (pttx-3::egfp::lgg-1;pttx-3::mCh)	(Stavoe et al., 2016)	DCR4750
C. elegans: unc-13(e450);olaIs35	(Hill et al., 2019)	DCR5581
C. elegans: atg-9(wy56);olaIs35	(Stavoe et al., 2016)	DCR4851
C. elegans: unc-26(s1710);olaIs35	This paper	DCR6122
C. elegans: unc-26(s1710);atg-9(wy56);olaIs35	This paper	DCR8128
C. elegans: atg-9(ΔAP);olaIs35	This paper	DCR8868
C. elegans: unc-26(R216Q) IV	This paper	DGR7333
C. elegans: unc-26(R216Q);olaIs34	This paper	DGR7337
C. elegans: sac-2/W09C5.7(gk346019) I	Caenorhabditis Genetics Center	VG20557
C. elegans: sac-2/W09C5.7(gk927434) I	Caenorhabditis Genetics Center	VG41013
C. elegans: sac-2/W09C5.7(gk346019);olaIs34	This paper	DGR6730
C. elegans: sac-2/W09C5.7(gk927434);olaIs34	This paper	DGR6731
C. elegans: unc-26(s1710);sac-2(gk346019);olaIs34	This paper	DGR7077
C. elegans: unc-26(s1710); sac-2(gk927434);olaIs34	This paper	DGR7062
C. elegans: unc-26(R216Q); sac-2(gk346019);olaIs34	This paper	DGR8871
C. elegans: olaex4504 [DAGR3699 (pttx-3:gfp:chc-1) (5ng/μl)]	This paper	DGR7480
C. elegans: unc-26(R216Q);olaex4504	This paper	DGR7748

Neuron. Author manuscript; available in PMC 2023 March 02.

REAGENT or RESOURCE	SOURCE	IDENTIFIER
Chemicals		
C. elegans: *olaex4016* [DAGR2716 (pttx-3::sng-1::gfp) (15ng/µl) + DAGR922 (pttx-3::atg-9::mCh) (20ng/µl)]	This paper	DGR6704
C. elegans: unc-26(R216Q);olaex4016	This paper	DGR7769
C. elegans: unc-26(R216Q);olaex4290;olaIs34	This paper	DGR8586
Recombinant DNA		
Plasmid: pttx-3::atg-9::gfp	(Liang et al., 2012)	DAGR808
Plasmid: pttx-3::atg-9::mCh	This paper	DAGR922
Plasmid: pttx-3::sng-1::bfp	This paper	DAGR2739
Plasmid: pttx-3::mCh::rab-3	(Colon-Ramos et al., 2007)	DAGR18
Plasmid: punc-14::atg-9::gfp	(Stavoe et al., 2016)	DAGR1821
Plasmid: pttx-3::unc-26	This paper	DAGR4860
Plasmid: pttx-3::sng-1::gfp	This paper	DAGR2716
Plasmid: pttx-3::sng-1::bfp	This paper	DAGR2739
Plasmid: pttx-3::aman-2::gfp	This paper	DAGR941
Plasmid: pttx-3::tgn-38::mCh	This paper	DAGR3393
Plasmid: pttx-3::sp12::gfp	(Hill etal., 2019)	DGR930
Plasmid: pttx-3::tomm-20::gfp	(Hill etal., 2019)	DAGR1617
Plasmid: pttx-3::gfp::lgg-1	(Stavoe et al., 2016)	DAGR1321
Plasmid: pttx-3::bfp::chc-1	This paper	DAGR2877
Plasmid: pttx-3:gfp:chc-1	This paper	DAGR3699
Antibodies		
Rabbit polyclonal anti-GFP	Abcam	Cat#ab6556; RRID: AB_305564
Rabbit monoclonal anti-ATG9A	Abcam	Cat#ab108338; RRID: AB_10863880
Mouse monoclonal anti-Bin1 (Amphiphysin2)	Upstate/Millipore	Cat#05–449; RRID: AB_309738
Guinea Pig polyclonal anti-VGAT	Gaibiochem	Cat#676780; RRID: AB_212625
Mouse monoclonal anti-Transferrin Receptor	Invitrogen/Thermo Fisher	Cat#13–6800; RRID: AB_86623

REAGENT or RESOURCE	SOURCE	IDENTIFIER
Chemicals		
Mouse monoclonal anti-Dynamin	BD Transduction Laboratories/BD Biosciences	Cat#610246; RRID: AB_397641
Rabbit polyclonal anti-beta-Tubulin	Invitrogen/Thermo Fisher	Cat#PA1–21153; RRID: AB_561870
Software and Algorithms		
Voiocity	Improvision by Perkin Elmer	N/A
Fiji	(Schindelin et al., 2012)	https://imagej.net/Fiji/Downioads
Prism	Graphpad Software Inc	https://www.graphpad.com/
Adobe Illustrator	Adobe	https://www.adobe.com/products/iiiustrator.html
Adobe Photoshop	Adobe	https://www.adobe.com/products/photoshop.html
MATLAB	MathWorks	https://www.mathworks.com/products/matiab.html
TrakEM2	(Cardona et al., 2012)	https://imagej.net/TrakEM2
ApE	M. Wayne Davis	https://jorgensen.bioiogy.utah.edu/wayned/ape/
Deposited Data		
Hippocampal Neuron Culture Protocol	Protocols.io, ASAP Collaborative Research Network	https://dx.doi.org/10.17504/protocols.io.b2deqa3e
Immunofluorescence Protocol	Protocols.io, ASAP Collaborative Research Network	https://dx.doi.org/10.17504/protocols.io.b2c7qazn
Dynamin Conditional Knockout Protocol	Protocols.io, ASAP Collaborative Research Network	https://dx.doi.org/10.17504/protocols.io.b2ddqa26
Surface Protein Biotinylation Protocol	Protocols.io, ASAP Collaborative Research Network	https://doi.org/10.17504/protocols.io.b2c8qazw
Code to Quantify Expressivity of ATG-9::GFP Subsynaptic Foci at the Presynaptic Region	GitHub	https://github.com/yangsisi76/Quantify-distribution-of-cell-structures.
Other		

REAGENT or RESOURCE	SOURCE	IDENTIFIER
Chemicals		
Sample transfer box	Custom, Yale machine shop	N/A
Diamond sectioning knife (Ultra 45°,4mm)	Diatome	N/A
Diamond trimming knife (45°)	Diatome	N/A
Aclar sheets 200 um (7.8mil)	EMS	Cat#50425
Chang embedding mold	EMS	Cat#70910
Nickel slot grids	EMS	Cat#FCF2010-Ni
Field Electron and Ion Company (FEI) Tecnai Biotwin	FEI	N/A
Flow-through rings	Leica Microsystems	Cat#16707157
Leica EM AFS2	Leica Microsystems	N/A
Leica EM HPM 100	Leica Microsystems	N/A
Leica EM UG7	Leica Microsystems	N/A
Leica plastic capsules (D5 x H15)	Leica Microsystems	Cat#16702738
Universal container for plastic capsules	Leica Microsystems	Cat#16702735
UltraView VoX spinning disc confocal microscope with a 60x CFI Plan Apo VC, NA 1.4, oil objective on a NikonTi-E stand	PerkinElmer	N/A
Specimen Carrier Type A	Technotrade International	Part# 241
Specimen Carrier Type B	Technotrade International	Part# 242
Talos L120G	Thermo Fisher	N/A
Gene Frame Adhesive Frames	Thermo Scientific	Cat#AB-0576